

# Pair Production in time-dependent Electric field at Finite times

Deepak Sah<sup>\*1,2</sup> and Manoranjan P. Singh<sup>1,2</sup>

<sup>1</sup>*Homi Bhabha National Institute, Training School Complex,  
Anushakti Nagar, Mumbai 400094, India*

<sup>2</sup>*Theory and Simulations Lab, Raja Ramanna Centre  
for Advanced Technology, Indore-452013, India*

## Abstract

We investigate the finite-time behavior of pair production from the vacuum by a time-dependent Sauter pulsed electric field using the spinor quantum electrodynamics (QED). In the adiabatic basis, the one-particle distribution function in momentum space is determined by utilizing the exact analytical solution of the Dirac equation. By examining the temporal behavior of the one-particle distribution function and the momentum spectrum of created pairs in the sub-critical field limit ( $E_0 = 0.2E_c$ ), we observe oscillatory patterns in the longitudinal momentum spectrum(LMS) of particles at finite times. These oscillations arise due to quantum interference effects resulting from the dynamical tunneling. Furthermore, we derive an approximate and simplified analytical expression for the distribution function at finite times, which allows us to explain the origin and behavior of these oscillations. Additionally, we discuss the role of the vacuum polarization function and its counter term to the oscillations in LMS vacuum excitation. We also study the time evolution of the transverse momentum spectrum (TMS), which shows interesting features at finite time.

PACS numbers:

Keywords:

---

\* Corresponding author.

E-mail address: deepakk@rrcat.gov.in (Deepak).

## I. INTRODUCTION

The concept of pair production in an electromagnetic field has its roots in the mid-1920s after the invention of quantum mechanics, with the formulation of the relativistic wave equation for electrons by Paul Dirac in 1928 [1]. The Dirac Sea model was proposed to explain the enigma of negative energy solutions. F. Sauter's work in 1931 demonstrated that strong electric fields can lead to pair creation through tunneling with exponential suppression [2]. This paved the way for quantum field theory, recognizing the vacuum as a polarizable medium influenced by constant fluctuations. In 1935, W. Heisenberg and H. Euler further explored the peculiarities of the Dirac equation, revealing non-linear modifications in Maxwell's equations due to the interaction of electromagnetic fields with the electron vacuum loop[3]. J. Schwinger's groundbreaking work in 1951 precisely calculated the imaginary part of the one-loop effective Lagrangian in the presence of a static electric field [4]. As a result of his seminal work, the phenomenon of vacuum pair creation by electric fields has since become widely known as the Schwinger effect, and it is also famously referred to as the Sauter-Schwinger effect in recognition of F. Sauter's prior work on solving the Dirac equation in the presence of an electric field [5]. Schwinger's pioneering calculation opened up new avenues of research in quantum field theory and has profoundly impacted our understanding of particle physics in the presence of strong fields. This extraordinary property of quantum vacuum producing spontaneous particle-antiparticle pairs has far-reaching implications for understanding the generation of particle-antiparticle pairs in the presence of a strong electric field [6]; particle creation in the expanding universe[7]; black hole evaporation as a result of Hawking radiation [8, 9]; and Unruh radiation, in which particle production is seen by an accelerating observer[10, 11]. The study of generating electron-positron pairs through a spatially constant electrical background field was extended to the electric field with various time dependences. In the 1970s, researchers explored the occurrence of pair production from the vacuum in the presence of an oscillating time-dependent electric field [12, 13]. Their investigations revealed different qualitative behaviors for this process under various interaction regimes. The interaction regimes can be distinguished by the value of the dimensionless Keldysh parameter  $\gamma = \frac{m\omega}{|e|E_0}$  [14], with field amplitude  $E_0$ , field frequency  $\omega$ , electron charge  $e$  and mass  $m$ . When  $\gamma \gg 1$ , the process probability shows a perturbative power-law scaling with field intensity. Instead, for  $\gamma \ll 1$ , it exhibits a manifestly non-perturbative exponential dependence on  $\frac{1}{E_0}$ , similar to the case of a constant electric field [15]. Particle production in a spatially homogeneous single pulse of an electric field has been explored [16, 17], and methods for tackling particle creation in an arbitrary time-dependent electric field have been developed [16, 18, 19]. Because a single pulse of an electric field is an idealized

form of an electric field created by two colliding laser beams, particle generation in an alternating electric field has been explored for a more realistic scenario [20, 21]. However, it was found that the mass of the created particle, via the Schwinger mechanism, exponentially suppresses the pair generation rate, necessitating a very strong electric field to observe this phenomenon. Therefore, this event has not yet been the subject of any experimental observations. This makes it unclear how well theoretical prediction captures the physics of pair production. However, the study of pair production in strong electric fields subject has attracted sustained interest from theoreticians in recent years due to the extraordinary progress in the development of the ultra-intense lasers technique and the strong field QED experimental studies that are planned at upcoming high-intensity laser facilities, such as the European X-Ray Free-Electron Laser [22], the Extreme-Light Infrastructure [23, 24], the Exawatt Center for Extreme Light Studies [25]. The electric field strength is fast getting closer to the critical value. Additionally, it is suggested that the Schwinger mechanism can be indirectly tested in the condensed matter system of a single monolayer of graphene, where the electrons are roughly characterized by the massless pseudo-relativistic Dirac equation [26–28].

Particle production can be viewed as evolving a quantum system from an initial equilibrium configuration to a new final equilibrium configuration via an intermediate non-equilibrium evolution caused by a strong field background. In intermediate non-equilibrium states, when matter fields interact with a time-dependent external field, the classical Hamiltonian loses its time translation invariance, leading to various choices for annihilation and creation operators (and consequently, the vacuum) in the Fock quantization. This lack of uniqueness of the vacuum state poses challenge in describing the evolution of the vacuum resulting in the creation of particle-antiparticle pairs as a function of time. Various vacuum choices have been explored in the literature, and the selection depends on the specific properties of the system under study and the quantum theory adopted. Adiabatic vacua are commonly employed in cosmology and the context of the Schwinger effect [29]. These adiabatic modes are established using a semiclassical WKB-type approximation. Reference mode functions are chosen as plane waves [30], proving particularly useful when the external background field changes slowly over time. Parker was among the first to propose a prominent alternative known as adiabatic vacua [31]. Subsequently, Leders and Roberts formalized Parker’s proposal in [32]. In this standard approach, the asymptotic analysis of particle states in the remote past ( or in-states /before the external field is switched on ) and future (or out-states/long after the interaction with the external field has finished) is well understood using the quantum field operator expression in terms of creation and annihilation operators, connected to one-particle states in both the present and the future. Then, using the relationship between the two sets of operators in the

past and future, we can derive an equation for the S-matrix of the process. This equation, in turn, provides the number of particles produced throughout the process. A variety of methodologies have been devised to investigate pair production in external fields. These techniques encompass the proper-time method [4, 33], the canonical method[34], Green's function methods [35], semi-classical tunneling [9], the Schrödinger-Functional approach[36], functional techniques [37, 38], mean-field treatment[39], and worldline instantons techniques [40, 41]. In the literature [42, 43], pair production in an intense laser field is studied using analytical ( or numerical) calculations and theoretical predictions about the pair-production rates as time averages over an infinite period of time, and these studies only focus on understanding the pair formation at the asymptotic time final equilibrium state. This idea, however, is not completely good enough for understanding pair production, at least theoretically, for several reasons. Firstly, it is rarely mentioned how pair production processes from vacuum change over time. This raises the question: Can particles manifest instantly during pair production? And lastly, can these times at which the formation of physical pairs occur be accessed in experiments? Motivated by these ideas, we provide a way of understanding the dynamics of pair production at all times. We look for the evolution of the quantum system at some initial time  $t_0$  in the vacuum state, but now what will be the properties of the quantum system at finite time  $t$ ? What happens to the system properties at all finite times? For that, the temporal evolution of particle distribution function in momentum space is good enough observable to give information about the asymptotic states of the quantum field but also give a complete description of the process when the matter field and the strong field background are still interacting. Information about the properties of the vacuum state before the production of real pairs unveils a previously undiscovered dimension in quantum non-equilibrium physics, thus exerting influence across various research domains concerning the emergence of quasi-particles. These specific time-dependent vacuum states poses questions about the physical interpretation of time-dependent observables related to pair production studies and the discussion in the literature is still open [44, 45]. Secondly, can we provide the physical meaning of the possible definition of the number of particles in terms of the number of particles measured well after the finite time  $t$  at which the external background has been switched off? Studied by various authors who have derived the adiabatic number of pairs created after a time  $T$  (where  $T$  exceeds the electric field pulse duration)[35, 46–48], this provides a reliable approximation for measuring the actual pairs. The second motivation for our work focuses on the possibility of the formation of real pairs at the finite time when the electric field nearly vanishes, which may be experimentally accessible in the future. In the present work, we consider the production of electron-positron pairs from the

vacuum in a time-varying, spatially uniform pulsed electric field given by  $E(t) = E_0 \text{sech}^2\left(\frac{t}{\tau}\right)$ , with amplitude  $E_0$  and pulse duration  $\tau$ . Such background field has received extensive attention in the literature [16, 27, 35, 49–52], with a focus on the asymptotic behavior of the probability of pair production. This naturally raises questions about the instantaneous appearance of particles in pair production and their behavior at intermediate times when using a dynamical formalism. To this end, we study the evolution of the one-particle distribution function,  $f(\mathbf{p}, t)$  in momentum space, which is rigorously derived from QED by canonical quantization of the Dirac field and subsequent Bogoliubov transformation to a quasi-particle representation. In the case of a time-dependent Sauter-pulse electric field, the exact solution of the one-particle Dirac equation is possible, and using it, we analytically compute the particle distribution function,  $f(\mathbf{p}, t)$  in terms of Gauss-Hypergeometric function. It is well known that pair production from vacuum undergoes three different stages of evolution: quasidelectron-positron plasma (QEPP), the transient stage, and the final residual electron-positron plasma (REPP) stage. By temporal evolution of  $f(\mathbf{p}, t)$ , we find that the occurrence of three stages is influenced by longitudinal and transverse momentum values qualitatively and quantitatively. Next, We analyze the created particles' longitudinal momentum spectrum (LMS) at finite times. In the tunneling regime ( $\gamma < 1$ ), we observe oscillatory structure in the LMS at time  $t > 2\tau$ , and this oscillation pattern continuously changes from  $t > 2\tau$  up to  $t < 6\tau$  for  $\gamma < 1$ . This oscillation behavior at finite time clearly illustrates the quantum interference effects associated with particle production, as explained in terms of the vacuum polarisation function,  $u(\mathbf{p}, t)$  and its counter-part depolarisation function,  $v(\mathbf{p}, t)$  using dynamical tunneling in the momentum-space representation. We emphasize that the oscillations seen in the LMS are not artifacts but rather possess significant physical relevance. In the multi-photon regime, we see that LMS at finite time near  $t = 3\tau$  shows the multi-modal structure. Additionally, we explored how the transverse momentum affects LMS and discovered that the oscillatory behavior is contingent upon the value of  $p_\perp$  at that time. Subsequently, we analyzed the temporal progression of TMS of generated pairs, offering valuable insights into the pair production process.

This article is organized as follows: In Sec.II detailed the theoretical formulation is given. This largely follows the derivation from [53, 54]. In Sec. III, we present expressions for the particle momentum distribution function using the exact analytical solution for the mode function in the case of a Sauter-pulsed electric field. Results are discussed in Sec. IV. The article is concluded in Sec. V.

Throughout the paper, we use natural units and set  $\hbar = c = m = |e| = 1$ , the electric charge  $e < 0$ , and express all variables in terms of the electron mass unit.

## II. THEORY

In this section, we review the canonical quantization method within the framework of a strong electric field, as discussed in [54]. Utilizing this formalism provides us with extensive insights into pair production phenomena, including crucial information on particle number and momentum distribution at each moment. This enables us to articulate the intricate processes involved in the creation and annihilation of electrons or positrons. To commence our exploration, we begin by establishing solutions for the one-particle scenario governed by the Dirac equation in the presence of such a field. We start by writing the Dirac equation for a particle in an electromagnetic field, which takes the following form:

$$(i\gamma^\mu \partial_\mu - e\gamma^\mu A_\mu - m)\Psi(\mathbf{x}, t) = 0. \quad (1)$$

where,  $A^\mu$  is the four-vector electromagnetic potential,  $m$  is the mass of electron,  $e$  is the charge of the electron,  $\Psi(\mathbf{x}, t)$  is the four-component spinor. For  $\gamma$ -matrices we chose the weyl basis [55]

$$\gamma^0 = \begin{pmatrix} \mathbb{I} & 0 \\ 0 & -\mathbb{I} \end{pmatrix}, \gamma^i = \begin{pmatrix} 0 & -\sigma^i \\ \sigma^i & 0 \end{pmatrix}, i = 1, 2, 3, \quad (2)$$

where,  $\mathbb{I}$  is the identity matrix and  $\sigma^i$  are the Pauli matrices. The  $\gamma$  matrices satisfy the anti-commutation relations:

$$\{\gamma^\mu, \gamma^\nu\} = 2g^{\mu\nu}, \quad (3)$$

with the metric tensor,

$$g^{\mu\nu} = \text{diag}(1, -1, -1, -1) \quad (4)$$

where,  $\mu, \nu = 0, 1, 2, 3$ .

Four coupled differential equations result from the Dirac equation for the spinor, and it is typically challenging to find precise analytical solutions in the presence of external fields. Feynmann and Gell-Mann were able to circumvent this difficulty by taking into account a two-component form of the Dirac equation [56]. Accordingly, we turn this equation into a second-order differential equation by assuming the existence of a bispinor  $\chi(\mathbf{x}, t)$  such that

$$\Psi(\mathbf{x}, t) = (i\gamma^\nu \partial_\nu - e\gamma^\nu A_\nu + m)\chi(\mathbf{x}, t). \quad (5)$$

and inserting Eq. (5) into Eq. (1), it follows that  $\chi(\mathbf{x}, t)$  satisfies the quadratic Dirac equation

$$[(i\partial_\mu - eA_\mu)^2 - \frac{e}{2}\sigma^{\mu\nu}\mathcal{F}_{\mu\nu} - m^2]\chi(\mathbf{x}, t) = 0 \quad (6)$$

where,  $\mathcal{F}_{\mu\nu} = \partial_\mu A_\nu - \partial_\nu A_\mu$  is the field strength tensor,  $\sigma^{\mu\nu} = \frac{i}{2}[\gamma^\mu, \gamma^\nu]$  and  $\chi(\mathbf{x}, t)$  is a four component spinor.

Here, we consider the case where the electromagnetic field tensor is  $\mathcal{F}^{\mu 0} = (0, 0, 0, E(t))$  with  $E(t)$  linearly polarized time-dependent quasi-classical spatially uniform electric field along the  $z$ -axis and the corresponding four-vector potential  $A^\mu(\mathbf{x}, t) = (0, \mathbf{A}(t)) \equiv (0, 0, 0, A(t))$ , with an arbitrary  $A(t)$  such that  $E(t) = -\frac{dA(t)}{dt}$ .

Then, Now Eq.(6) can be simplified to

$$(\square + e^2 A^2(t) + 2iA(t)\partial_3 - ie\partial_t A(t)\gamma^0\gamma^3 + m^2)\chi(\mathbf{x}, t) = 0. \quad (7)$$

Here,  $\square = \partial_\mu \partial^\mu$  is D'Alembert operator. Spatial homogeneity solutions of the form

$$\chi(\mathbf{x}, t) = e^{i\mathbf{p}\cdot\mathbf{x}}\chi_p(t), \quad (8)$$

where,  $\chi_p(t)$  is independent of the position  $\mathbf{x}$  and we label it by momentum of a particle  $\mathbf{p}$ .

Now, Eq. (7) becomes

$$(\partial_t^2 + ieE(t)\gamma^0\gamma^3 + \omega^2(\mathbf{p}, t))\chi_p(t) = 0. \quad (9)$$

with

$$\omega(\mathbf{p}, t) = \sqrt{\epsilon_\perp^2(p_\perp) + P^2(p_\parallel, t)}, \quad \epsilon_\perp(p_\perp) = \sqrt{m^2 + p_\perp^2}, \quad P(p_\parallel, t) = p_\parallel - eA(t) \quad (10)$$

Here,  $p_\perp = \sqrt{p_1^2 + p_2^2}$  is the modulus of the vector  $\mathbf{p}_\perp$  perpendicular to the field, and  $p_\parallel = p_3$  is the momentum component to the field direction.

Now we expand the function  $\chi_p(t)$  in the basis of eigenvectors of  $\gamma^0\gamma^3$ . The matrix representation of  $\gamma^0\gamma^3$  is

$$\gamma^0\gamma^3 = \begin{pmatrix} \mathbb{I} & 0 \\ 0 & -\mathbb{I} \end{pmatrix} \begin{pmatrix} 0 & \sigma^3 \\ -\sigma^3 & 0 \end{pmatrix} = \begin{pmatrix} 0 & \sigma^3 \\ \sigma^3 & 0 \end{pmatrix}, \quad (11)$$

making it easy to recognize the eigenvector. They are given by

$$R_1 = \begin{pmatrix} 1 \\ 0 \\ 0 \\ 0 \end{pmatrix}, \quad R_2 = \begin{pmatrix} 0 \\ 0 \\ 0 \\ 1 \end{pmatrix}, \quad R_3 = \begin{pmatrix} 0 \\ 1 \\ 0 \\ 0 \end{pmatrix}, \quad R_4 = \begin{pmatrix} 0 \\ 0 \\ 1 \\ 0 \end{pmatrix}, \quad (12)$$

Two doubly degenerate eigenvectors exist for  $\gamma^0\gamma^3$  with  $R_1, R_2$  having eigenvalue '1' and  $R_3, R_4$  having eigenvalue '-1'. However, it turns out that picking one of them is sufficient [53]. Now, we shall seek the solutions of Eq. (9) in the form

$$\chi_p(t) \equiv \chi_{pr}(t) = \psi_p(t)R_r, \quad (13)$$

where  $\gamma^0\gamma^3 R_r = R_r$ . Solving a differential equation for a scalar function  $\psi_{\mathbf{p}}(t)$  simplifies the problem,

$$\left(\partial_t^2 + ieE(t) + \omega^2(\mathbf{p}, t)\right)\psi_{\mathbf{p}}(t) = 0. \quad (14)$$

Now, let's examine the resulting solutions. It follows from Eq. (14) that, in vanishing electric field, as  $t \rightarrow -\infty$ , the term  $\omega(\mathbf{p}, t)$  becomes independent of time  $\omega(\mathbf{p})$  and the scalar function  $\psi(\mathbf{p}, t)$  satisfies the asymptotic equation,

$$\left(\partial_t^2 + \omega^2(\mathbf{p})\right)\psi_{\mathbf{p}}(t) = 0, \quad (15)$$

There are two linearly independent solutions to this time-dependent harmonic oscillator equation, which correspond to energy  $\pm\omega(\mathbf{p})$ . In what follows, we will label these solutions with superscripts  $\lambda = +$  and  $\lambda = -$ , respectively. Solutions of this equation are clearly given by plane waves, and thus

$$\psi_{\mathbf{p}}^{(\lambda)}(t) \underset{t \rightarrow -\infty}{\sim} e^{-i\lambda\omega(\mathbf{p})t}. \quad (16)$$

These solutions will be interpreted as describing an electron ( $\lambda = +$ ) and its anti-particle, i.e., a positron ( $\lambda = -$ ), in the electric field. Finally, the corresponding solutions of Eq. (7) have the form,

$$\chi_{\mathbf{p}r}^{(\lambda)}(\mathbf{x}, t) = e^{i\mathbf{p}\cdot\mathbf{x}}\psi_{\mathbf{p}}^{(\lambda)}(t)R_r, \quad (17)$$

those of the Dirac equation, however, are derived

$$\Psi_{\mathbf{p}r}^{(\lambda)}(\mathbf{x}, t) = \left[i\gamma^0\partial_t - \mathbf{p}\cdot\boldsymbol{\gamma} + eA(t)\gamma^3 + m\right]e^{i\mathbf{p}\cdot\mathbf{x}}\psi_{\mathbf{p}}^{(\lambda)}(t)R_r. \quad (18)$$

where the spinor solutions,  $\Psi_{\mathbf{p}r}^{(\lambda)}(\mathbf{x}, t)$  are normalised according to the product:

$$\int d^3\mathbf{x}[\Psi_{\mathbf{p}r}^{(\lambda)}(\mathbf{x}, t)]^\dagger\Psi_{\mathbf{p}'r'}^{(\lambda')}(\mathbf{x}, t) = (2\pi)^3\delta(\mathbf{p} - \mathbf{p}')\delta_{rr'}\delta_{\lambda\lambda'} \quad (19)$$

Hence, the newly constructed eigenstates of the Dirac equation representing an electron or positron in a time-dependent electric field provide a complete and orthonormal relation

$$\sum_{\lambda=\pm} \sum_{r=\pm} \int \frac{d^3\mathbf{p}}{(2\pi)^3} \Psi_{\mathbf{p}r}^{(\lambda)}(\mathbf{x}, t)[\Psi_{\mathbf{p}'r'}^{(\lambda)}(\mathbf{x}')]^\dagger = \delta(\mathbf{x} - \mathbf{x}'). \quad (20)$$

The Dirac fermion field operator  $\hat{\Psi}(\mathbf{x}, t)$  in the framework of second quantization is written in the form

$$\hat{\Psi}(\mathbf{x}, t) = \sum_r \int \frac{d^3\mathbf{p}}{(2\pi)^3} \left(\Psi_{\mathbf{p}r}^{(+)}(\mathbf{x}, t)\hat{b}_{\mathbf{p}r} + \Psi_{-\mathbf{p}r}^{(-)}(\mathbf{x}, t)\hat{d}_{\mathbf{p}r}^\dagger\right), \quad (21)$$



where  $\Psi_{pr}^{(\lambda)}(\mathbf{x}, t)$  are the single particle solutions of the Dirac equation, whereas  $\hat{b}_{pr}$  and  $\hat{d}_{pr}$  are the annihilation operators of electron and positron with momentum  $\mathbf{p}$  and spin  $r$ . The operators satisfy the standard fermionic anti-commutation relations,

$$\{\hat{b}_{pr}, \hat{b}_{p'r'}^\dagger\} = \{\hat{d}_{pr}, \hat{d}_{p'r'}^\dagger\} = \delta(\mathbf{p} - \mathbf{p}')\delta_{rr'}, \quad (22)$$

Then the  $\hat{\Psi}(\mathbf{x}, t)$  field operator also satisfies the anti-commutation relation,

$$\{\hat{\Psi}_n(\mathbf{x}, t), \hat{\Psi}_m^\dagger(\mathbf{x}', t)\} = (2\pi)^3 \delta(\mathbf{x} - \mathbf{x}')\delta_{mn}. \quad (23)$$

Now, the Hamiltonian can be calculated from the energy-momentum tensor which yields,

$$\hat{H}(t) = i \int \hat{\Psi}^\dagger(t, \mathbf{x}) \hat{\Psi}(t, \mathbf{x}) d^3\mathbf{x} \quad (24)$$

the diagonal and off-diagonal parts of the Hamiltonian are given as

$$\hat{H}_{diag}(t) = i \sum_r \int \frac{d^3\mathbf{p}}{(2\pi)^3} [\varepsilon_{\mathbf{p}}^{(++)}(t) \hat{b}_{pr}^\dagger \hat{b}_{pr} + \varepsilon_{\mathbf{p}}^{(--)}(t) \hat{d}_{-pr}^\dagger \hat{d}_{-pr}], \quad (25)$$

$$\hat{H}_{offdiag}(t) = i \sum_r \int \frac{d^3\mathbf{p}}{(2\pi)^3} [\varepsilon_{\mathbf{p}}^{(+-)}(t) \hat{b}_{pr}^\dagger \hat{d}_{-pr}^\dagger + \varepsilon_{\mathbf{p}}^{(-+)}(t) \hat{d}_{-pr} \hat{b}_{pr}], \quad (26)$$

where the factors  $\varepsilon_{\mathbf{p}}^{(\lambda\lambda')}(t)$  are expressed as

$$\varepsilon_{\mathbf{p}}^{(\lambda\lambda')}(t) = \begin{cases} \omega^2(\mathbf{p}, t) (\dot{\psi}_{\mathbf{p}}^{(\lambda)}(t) [\psi_{\mathbf{p}}^{(\lambda)}(t)]^* - \psi_{\mathbf{p}}^{(\lambda)}(t) [\dot{\psi}_{\mathbf{p}}^{(\lambda)}(t)]^*) + iP(t) (|\dot{\psi}_{\mathbf{p}}^{(\lambda)}(t)|^2 + \omega^2(\mathbf{p}, t) |\psi_{\mathbf{p}}^{(\lambda)}(t)|^2) & \text{if } \lambda = \lambda', \\ \omega^2(\mathbf{p}, t) (\dot{\psi}_{\mathbf{p}}^{(\lambda)}(t) \psi_{-\mathbf{p}}^{(\lambda')}(t) - \psi_{\mathbf{p}}^{(\lambda)}(t) \dot{\psi}_{-\mathbf{p}}^{(\lambda')}(t)) + iP(t) (\dot{\psi}_{\mathbf{p}}^{(\lambda)}(t) \dot{\psi}_{-\mathbf{p}}^{(\lambda')}(t) + \omega^2(\mathbf{p}, t) \psi_{\mathbf{p}}^{(\lambda)}(t) \psi_{-\mathbf{p}}^{(\lambda')}(t)) & \text{if } \lambda \neq \lambda', \end{cases} \quad (27)$$

As the above Hamiltonian, has non-vanishing off-diagonal elements, the positive and negative energy modes mix, and thus, clear interpretation in terms of particles and antiparticles is difficult. In order to calculate the spectrum, the Hamiltonian is diagonalized by a basis transformation, to the quasi-particle representation through the new time-dependent operators  $\hat{B}_{pr}(t)$  and  $\hat{D}_{pr}(t)$ . The relation between the  $\hat{b}_{pr}$ ,  $\hat{d}_{pr}$  and  $\hat{B}_{pr}(t)$ ,  $\hat{D}_{pr}(t)$  operators is given by the Bogoliubov transformation

$$\hat{B}_{pr}(t) = \alpha_{\mathbf{p}}(t) \hat{b}_{pr} + \beta_{\mathbf{p}}(t) \hat{d}_{-pr}^\dagger, \quad (28)$$

$$\hat{D}_{pr}(t) = \alpha_{-\mathbf{p}}(t) \hat{d}_{pr} - \beta_{-\mathbf{p}}(t) \hat{b}_{-pr}^\dagger. \quad (29)$$

Now, the instantaneous vacuum state is defined as  $\hat{B}_{pr}(t)|0_t\rangle = 0$  and  $\hat{D}_{pr}(t)|0_t\rangle = 0$ .

The transformation preserves the anti-commutation relations of the creation and annihilation operators provided that, at every time  $t$ , unknown functions  $\alpha_{\mathbf{p}}(t)$  and  $\beta_{\mathbf{p}}(t)$  satisfy the condition,

$$|\alpha_{\mathbf{p}}(t)|^2 + |\beta_{\mathbf{p}}(t)|^2 = 1. \quad (30)$$

In the new basis  $\hat{\Psi}(\mathbf{x}, t)$  can be written as:

$$\hat{\Psi}(\mathbf{x}, t) = \sum_r \int \frac{d^3\mathbf{p}}{(2\pi)^3} [\Phi_{pr}^{(+)}(\mathbf{x}, t) \hat{B}_{pr}(t) + \Phi_{-pr}^{(-)}(\mathbf{x}, t) \hat{D}_{pr}^\dagger(t)], \quad (31)$$

with the spinors  $\Phi_{pr}^{(\lambda)}(\mathbf{x}, t)$  such that

$$\Phi_{pr}^{(+)}(\mathbf{x}, t) = \alpha_{\mathbf{p}}^*(t) \Psi_{pr}^{(+)}(\mathbf{x}, t) + \beta_{\mathbf{p}}^*(t) \Psi_{pr}^{(-)}(\mathbf{x}, t), \quad (32)$$

$$\Phi_{pr}^{(-)}(\mathbf{x}, t) = \alpha_{\mathbf{p}}(t) \Psi_{pr}^{(-)}(\mathbf{x}, t) - \beta_{\mathbf{p}}(t) \Psi_{pr}^{(+)}(\mathbf{x}, t). \quad (33)$$

It follows from here that  $\Phi_{pr}^{(\lambda)}(\mathbf{x}, t)$  should have the same spinor form as  $\Psi_{pr}^{(\lambda)}(\mathbf{x}, t)$ . Accordingly,

$$\Phi_{pr}^{(\lambda)}(\mathbf{x}, t) = [i\gamma^0 \partial_t - \mathbf{p} \cdot \boldsymbol{\gamma} + eA(t)\gamma^3 + m] e^{i\mathbf{p} \cdot \mathbf{x}} \phi_{\mathbf{p}}^{(\lambda)}(t) R_r, \quad (34)$$

where,  $\phi_{\mathbf{p}}^{(\lambda)}(t)$  are unknown functions. The function  $\phi_{\mathbf{p}}^{(\lambda)}(t)$  are the mode functions in the quasi-particle representation, which are chosen according to the ansatz,

$$\phi_{\mathbf{p}}^{(\lambda)}(t) = \frac{e^{-i\lambda\Theta_{\mathbf{p}}(t)}}{\sqrt{2\omega(\mathbf{p}, t)(\omega(\mathbf{p}, t) - \lambda P(t))}} \quad (35)$$

The functions  $\phi_{\mathbf{p}}^{(\lambda)}(t)$  are chosen such that they coincide with the mode functions  $\psi_{\mathbf{p}}^\lambda(t)$  in the case of a vanishing vector potential. Now, combining Eqs. (18), (32), (33), and (34), we obtain that

$$\psi_{\mathbf{p}}^{(+)}(t) = \alpha_{\mathbf{p}}(t) e^{-i\Theta_{\mathbf{p}}(t)} \phi_{\mathbf{p}}^{(+)}(t) - \beta_{\mathbf{p}}^*(t) e^{i\Theta_{\mathbf{p}}(t)} \phi_{\mathbf{p}}^{(-)}(t), \quad (36)$$

$$\psi_{\mathbf{p}}^{(-)}(t) = \beta_{\mathbf{p}}(t) e^{-i\Theta_{\mathbf{p}}(t)} \phi_{\mathbf{p}}^{(+)}(t) + \alpha_{\mathbf{p}}^*(t) e^{i\Theta_{\mathbf{p}}(t)} \phi_{\mathbf{p}}^{(-)}(t). \quad (37)$$

with the accumulated dynamical phase,  $\Theta_{\mathbf{p}}(t_0, t) = \int_{t_0}^t dt' \omega(\mathbf{p}, t')$ . and the coefficients  $\alpha_{\mathbf{p}}(t)$  and  $\beta_{\mathbf{p}}(t)$  are given by

$$\alpha_{\mathbf{p}}(t) = i\phi_{\mathbf{p}}^{(-)}(t) \epsilon_{\perp}(p_{\perp}) e^{i\Theta_{\mathbf{p}}(t)} (\partial_t - i\omega(\mathbf{p}, t)) \psi_{\mathbf{p}}^{(+)}(t) \quad (38)$$

$$\beta_{\mathbf{p}}(t) = -i\phi_{\mathbf{p}}^{(+)}(t) \epsilon_{\perp}(p_{\perp}) e^{-i\Theta_{\mathbf{p}}(t)} (\partial_t + i\omega(\mathbf{p}, t)) \psi_{\mathbf{p}}^{(+)}(t) \quad (39)$$

From the above equations, if we know  $\psi_{\mathbf{p}}(t)$  from a solution of differential Eq. (14) for a specific electric field, we can find out the Bogolyubov transformation coefficients and correspondingly momentum distribution function of the created particle. The occupation number of electrons in

the given eigenmode  $\mathbf{p}r$  of the fermionic field using the time-dependent creation and annihilation operators for the initial vacuum state is defined as

$$f_r(\mathbf{p}, t) = \langle 0_{in} | \hat{B}_{\mathbf{p}r}^\dagger(t) \hat{B}_{\mathbf{p}r}(t) | 0_{in} \rangle \quad (40)$$

Similarly, the occupation number of the positron is given by

$$\bar{f}_r(-\mathbf{p}, t) = \langle 0_{in} | \hat{D}_{-\mathbf{p}r}^\dagger(t) \hat{D}_{-\mathbf{p}r}(t) | 0_{in} \rangle \quad (41)$$

Because of the charge conjugation invariance,

$$f_r(\mathbf{p}, t) = \bar{f}_r(-\mathbf{p}, t) \quad (42)$$

In the quasi-particle model,  $f_r(\mathbf{p}, t)$  and  $\bar{f}_r(-\mathbf{p}, t)$  will act as one-particle distribution functions [57]. Since the Hamiltonian Eq.(24) does not have any spin-dependent terms, the spin index( $r$ ) is dropped, and the distribution function

$$f(\mathbf{p}, t) = 2|\beta_{\mathbf{p}}(t)|^2 \quad (43)$$

where the factor ‘2’ corresponds to the spin degree of freedom. A possible way to find  $f(\mathbf{p}, t)$  is to solve Eq.(14) for  $\psi(t)$  and use it to solve for Bogoliubov coefficients to get one-particle distribution function.

### III. PAIR PRODUCTION IN SAUTER-PULSE ELECTRIC FIELD

A spatially uniform external background is a common approximation of the electromagnetic field near the focal region of two counter-propagating laser pulses along, say, the z-axis, generating a standing wave[58, 59]. In general, the pair-production process takes place close to the electric field maximum (comparable to the critical field limit), where the magnetic field vanishes. Despite the fact that laser fields typically include many optical cycles, in this case, we examine a relatively simple model of the external field made up of the Sauter profile, which can be thought of as an extremely short laser pulse.

$$E(t) = E_0 \text{sech}^2\left(\frac{t}{\tau}\right), \quad (44)$$

where,  $\tau$  is the duration of pulse and  $E_0$  is field strength. This electric field exponentially goes to zero for  $|t| \gg \tau$ . In the limit of  $\tau \rightarrow \infty$  the electric field becomes homogeneous in time. We can choose a gauge in which  $A_0 = 0$  and the vector potential associated with the electric field is  $(0, 0, A(t) = -\int dt E(t))$ . After the integration, we find the Sauter-type gauge potential,

$$A(t) = -E_0 \tau \tanh\left(\frac{t}{\tau}\right). \quad (45)$$

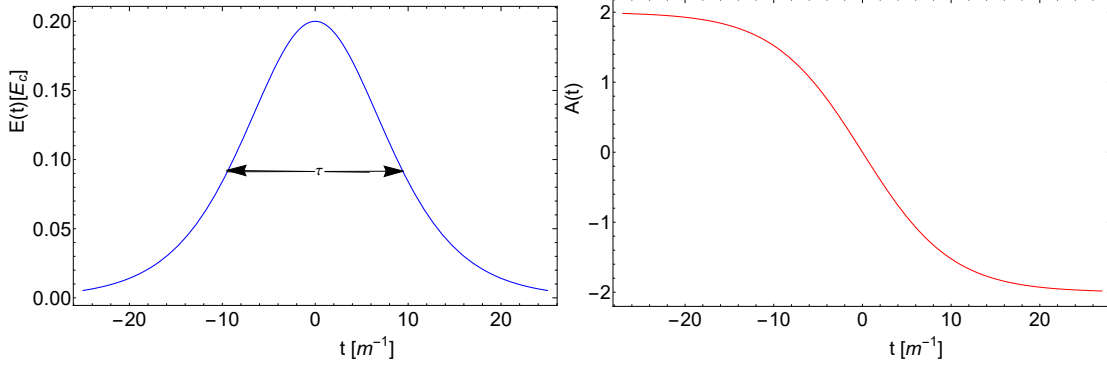


Figure 1: Temporal profile of the electric field (left) and the associated vector potential with the choice  $A(t = 0) = 0$  (right) for the field parameters  $E_0 = 0.2E_c$  and  $\tau = 10[m^{-1}]$ .

with  $A(t = 0) = 0$ .

The left panel of figure 1 shows the temporal profile of the electric field given by (44). Its peak height is attained at  $t = 0$ , its half height is reached at  $t = \pm 0.81\tau$ , and at  $t = \pm\tau$ , the pulse amplitude has already dropped to 41% of its peak height, followed by a further dramatic reduction well below 10% at  $t = \pm 2\tau$ .

Originally, Sauter [5] explored the Dirac equation within an inhomogeneous scalar potential  $V(z) = V_0 \text{sech}^2\left(\frac{z}{d}\right)$ . Since the problem is essentially reduced to solving a one-dimensional differential equation, the potential can also be addressed with a similar functional dependence on time, as given by Eq. (44). In 1970, the vacuum instability in a time-dependent Sauter-like electric field was initially examined by N. B. Narozhny et al. [16]. Subsequently, many researchers revisited this topic, finding it practical to test various approaches, including approximate methods, in the specific context being considered. Examples include Refs.[60–63], and the references therein. However, for the sake of completeness, we reproduce the essential steps and find out the expression for the one-particle distribution function,  $f(\mathbf{p}, t)$ , utilizing the solution of the differential equation.

Now, in the presence of external electric field Eq. (44) equation of motion for mode function Eq. (14) reads

$$\left(\partial_t^2 + iE_0 \text{sech}^2\left(\frac{t}{\tau}\right) + \omega^2(\mathbf{p}, t)\right)\psi_{\mathbf{p}}(t) = 0. \quad (46)$$

where we have skipped the irrelevant index  $\lambda$  of the mode function  $\psi_{\mathbf{p}}(t)$ . This equation is solved analytically by converting it into a hypergeometric differential equation. By changing the time

variable to  $y = \frac{1}{2} \left( 1 + \tanh \left( \frac{t}{\tau} \right) \right)$ , Additionally, we compute

$$\partial_t = (\partial_t y) \partial_y = \frac{2}{\tau} y(1-y) \partial_y \quad (47)$$

$$\partial_t^2 = \frac{4}{\tau^2} y(1-y) \partial_y y(1-y) \quad (48)$$

Now, Eq.(46) can be rewritten as

$$\left( \frac{4}{\tau^2} y(1-y) \partial_y y(1-y) \partial_y + \omega^2(\mathbf{p}, y) + 4iE_0 y(1-y) \right) \psi_{\mathbf{p}}(y) = 0. \quad (49)$$

Further, by using the following ansatz

$$\psi_{\mathbf{p}}(y) = y^k (1-y)^l \eta_{\mathbf{p}}(y) \quad (50)$$

with,  $k = \frac{-i\tau\omega_0}{2}$ ,  $l = \frac{i\tau\omega_1}{2}$ ,  $\omega_0^2 = m^2 + p_{\perp}^2 + (p_{\parallel} - eE_0\tau)^2$  and,  $\omega_1^2 = m^2 + p_{\perp}^2 + (p_{\parallel} + eE_0\tau)^2$  in Eq. (49), we have  $\eta_{\mathbf{p}}(y)$  satisfying the following hypergeometric differential equation [64]

$$\left( y(1-y) \partial_y^2 + (c - (a+b+1)y) \partial_y - ab \right) \eta_{\mathbf{p}}(y) = 0. \quad (51)$$

Here,

$$\begin{aligned} a &= -iE_0\tau^2 - \frac{i\tau\omega_0}{2} + \frac{i\tau\omega_1}{2} = i\zeta_1 \\ b &= 1 + iE_0\tau^2 - \frac{i\tau\omega_0}{2} + \frac{i\tau\omega_1}{2} = 1 + i\zeta_2, \\ c &= 1 - i\tau\omega_0 = 1 + i\zeta_3, \end{aligned} \quad (52)$$

$$P_0 = \sqrt{(p_{\parallel} - eE_0\tau)^2}, P_1 = \sqrt{(p_{\parallel} + eE_0\tau)^2}$$

The two linearly independent solutions of Eq.(51) are  $\eta_{\mathbf{p}}^{(\pm)}(y)$  which are analytic in the neighborhood of the singular point  $y = 0$

$$\eta_{\mathbf{p}}^{(+)}(y) = {}_2\mathcal{F}_1(a, b, c; y), \quad (53)$$

$$\eta_{\mathbf{p}}^{(-)}(y) = y^{1-c} (1-y)^{c-a-b} {}_2\mathcal{F}_1(1-a, 1-b, 2-c; y). \quad (54)$$

with  ${}_2\mathcal{F}_1(a, b, c; y)$  denoting the Gauss-hypergeometric function[64].

To get the mode functions  $\psi_{\mathbf{p}}^{(\pm)}(y)$  we have to resubstitute  $\eta_{\mathbf{p}}^{(\pm)}(y)$  in Eq.(50)

$$\psi_{\mathbf{p}}^{(+)}(y) = N^{(+)}(\mathbf{p}) y^k (1-y)^l {}_2\mathcal{F}_1(a, b, c; y), \quad (55)$$

$$\psi_{\mathbf{p}}^{(-)}(y) = N^{(-)}(\mathbf{p}) y^{-k} (1-y)^{-l} {}_2\mathcal{F}_1(1-a, 1-b, 2-c; y) \quad (56)$$

where  $N^{(\pm)}(\mathbf{p})$  as normalization constants. These constants are chosen such that

$$\psi_{\mathbf{p}}^{(\pm)}(y \rightarrow 0) = \phi_{\mathbf{p}}^{(\pm)}(y \rightarrow 0)$$

using the initial condition, we get

$$N^{(\pm)}(\mathbf{p}) = \frac{e^{\mp i\tilde{\Theta}_p(y_0,0)}}{\sqrt{2\omega_0(\omega_0 \mp P_0)}} \quad (57)$$

with accumulated phase,  $\tilde{\Theta}_p(y_0, 0) = \frac{2}{\tau} \int_{y_0}^0 dy' \frac{\omega(\mathbf{p}, y')}{y'(1-y')}$ .

### A. Particle distribution function

In order to get the one-particle distribution function using Eq. (43), we convert all functions in  $\beta(\mathbf{p}, t)$  given by Eq. (39) to the new time variable  $y$ . This transformation yields

$$|\beta(\mathbf{p}, y)|^2 = \frac{\epsilon_{\perp}^2(p_{\perp})}{2\omega(\mathbf{p}, y)(\omega(\mathbf{p}, y) - P(p_{\parallel}, y))} \left| \left( \frac{2}{\tau} y(1-y)\partial_y + i\omega(\mathbf{p}, y) \right) \psi^{(+)}(\mathbf{p}, y) \right|^2 \quad (58)$$

Using Eq. (56), the analytical expression for the one-particle distribution function in terms of the transformed time variable  $y$  can be written as

$$f(\mathbf{p}, y) = |N^+(\mathbf{p})|^2 \left| \left( \frac{\omega(\mathbf{p}, y) + P(p_{\parallel}, y)}{\omega(\mathbf{p}, y)} \right) \left[ \frac{2}{\tau} y(1-y) \frac{ab}{c} f_1 + i(\omega - (1-y)\omega_0 - y\omega_1) f_2 \right] \right|^2 \quad (59)$$

where,  $f_1 = {}_2F_1(1+a, 1+b, 1+c; y)$ ,  $f_2 = {}_2F_1(a, b, c; y)$ .

This expression for the time-dependent one-particle momentum distribution function gives information about the pair production at the various dynamical stages[65]. In this context, our focus is on examining the behavior of the distribution function from the initial QEPP stage to the final REPP through the transient stage. A thorough discussion of these findings is provided in detail in Sec. IV. In the next section, we derive the simple approximate relation for the distribution function which is valid for  $t \gg \tau$  (pulse width of the applied laser field). Furthermore, in order to analyze the characteristics of the vacuum polarisation effect during the formation of pairs, we derive vacuum polarization and depolarisation functions using the analytical expression of Bogoliubov coefficients in the proceeding subsection III B.

### B. Correlation function

Quantum Vacuum in the presence of an external electric field may be described by a complex correlation function [66]. It is defined as,

$$C(\mathbf{p}, t) = \langle 0 | \hat{D}_{-pr}^{\dagger}(t) \hat{B}_{pr}^{\dagger}(t) | 0 \rangle = 2\alpha_p^*(t) \beta_p(t) \quad (60)$$

$$C^*(\mathbf{p}, t) = \langle 0 | \hat{D}_{-pr}(t) \hat{B}_{pr}(t) | 0 \rangle = 2\beta_{\mathbf{p}}^*(t) \alpha_{\mathbf{p}}(t) \quad (61)$$

As can easily be seen, this function  $C(\mathbf{p}, t)$  consisting of creation operators for a particle and an anti-particle with the opposite momentum describes the process of production of  $e^-e^+$  pair. In several research articles [57, 66–69], the particle-antiparticle correlation function is redefined by incorporating the slowly varying component of the time-dependent creation and annihilation operators in adiabatic basis.

$$\hat{\mathcal{B}}_{pr}(t) = \hat{B}_{pr}(t) e^{-i\Theta_{\mathbf{p}}(t)}$$

$$\hat{\mathcal{D}}_{-pr}(t) = \hat{D}_{-pr}(t) e^{-i\Theta_{\mathbf{p}}(t)}$$

where,  $\Theta_{\mathbf{p}}(t) = \int^t dt' \omega(\mathbf{p}, t')$

So that,

$$\begin{aligned} C(\mathbf{p}, t) &= \langle 0 | \hat{\mathcal{D}}_{-pr}^\dagger(t) \hat{\mathcal{B}}_{pr}^\dagger(t) | 0 \rangle \\ &= e^{2i\Theta_{\mathbf{p}}(t)} \langle 0 | \hat{D}_{-pr}^\dagger(t) \hat{B}_{pr}^\dagger(t) | 0 \rangle \\ &= 2\alpha_{\mathbf{p}}^*(t) \beta_{\mathbf{p}}(t) e^{2i\Theta_{\mathbf{p}}(t)} \end{aligned} \quad (62)$$

Now, using the above relation for the pair correlation function in terms of the transformed time variable  $y$ , similar to finding out for one-particle distribution function,  $f(\mathbf{p}, t)$  in section III.

$$\begin{aligned} C(\mathbf{p}, t) &= |N^+(\mathbf{p})|^2 \frac{\epsilon_{\perp}^2}{\omega(\mathbf{p}, t)} \left( \frac{4}{\tau^2} y^2 (1-y)^2 \left| \frac{ab}{c} \right|^2 |f_1|^2 + (\omega^2(\mathbf{p}, t) - (y\omega_1 + (1-y)\omega_0)^2) |f_2|^2 \right. \\ &\quad \left. + i \frac{2}{\tau} y(1-y)(y\omega_1 + (1-y)\omega_0) \left( \frac{ab}{c} f_1 \bar{f}_2 - \frac{\bar{a}b}{\bar{c}} \bar{f}_1 f_2 \right) \right) \end{aligned} \quad (63)$$

As we know, the vacuum polarization effects play a crucial role in the process of pair production. This effect is defined through the functions  $u(\mathbf{p}, t) = \Re(C(\mathbf{p}, t))$  and  $v(\mathbf{p}, t) = \Im(C(\mathbf{p}, t))$  [66].

$$\begin{aligned} u(\mathbf{p}, t) &= |N^+(\mathbf{p})|^2 \frac{\epsilon_{\perp}^2}{\omega(\mathbf{p}, t)} \left( \frac{4}{\tau^2} y^2 (1-y)^2 \left| \frac{ab}{c} \right|^2 |f_1|^2 + (\omega^2(\mathbf{p}, t) - (y\omega_1 + (1-y)\omega_0)^2) |f_2|^2 \right. \\ &\quad \left. + \frac{2}{\tau} y(1-y)((1-y)\omega_0 + y\omega_1) \left( \Im\left(\frac{\bar{a}b}{\bar{c}} \bar{f}_1 f_2\right) - \Im\left(\frac{ab}{c} f_1 \bar{f}_2\right) \right) \right) \end{aligned} \quad (64)$$

$$v(\mathbf{p}, t) = |N^+(\mathbf{p})|^2 \frac{\epsilon_{\perp}^2}{\omega(\mathbf{p}, t)} \left( \frac{2}{\tau} y(1-y)((1-y)\omega_0 + y\omega_1) \left( \Re\left(\frac{ab}{c} f_1 \bar{f}_2\right) - \Re\left(\frac{\bar{a}b}{\bar{c}} \bar{f}_1 f_2\right) \right) \right) \quad (65)$$

The function  $u(\mathbf{p}, t)$  depicts vacuum polarization effects and pair production phenomena. The function  $v(\mathbf{p}, t)$  serves as counter terms to pair production, effectively representing pair annihilation in the vacuum excitation process. A comprehensive discussion of these insights is presented in detail in Sec. IV C.

### C. Approximate analytical expression for $f(\mathbf{p}, t)$ at finite time

To investigate the behavior of the function  $f(\mathbf{p}, t)$  in the limit  $t \gg \tau$ , we employ approximations based on the suitable expressions of the Gamma and the Gauss-hypergeometric functions. These approximations enable us to deduce a simplified analytical expression for  $f(\mathbf{p}, t)$ . First, we start with approximating the Gauss-hypergeometric function as  $y \rightarrow 1$ . It is crucial to ensure smooth convergence towards the limit of  ${}_2\mathcal{F}_1(a, b, c; y \rightarrow 1)$ . This task is complicated by the intricate nature of the variables  $a$ ,  $b$ , and  $c$  in this specific context, which makes it essential to exercise caution when dealing with this limit. Therefore, it is beneficial to transform the argument by substituting  $y$  with  $(1 - y)$ . This transition can be achieved using the following mathematical identity.

$$\begin{aligned} {}_2\mathcal{F}_1(a, b, c; z) &= \frac{\Gamma(c)\Gamma(c-a-b)}{\Gamma(c-a)\Gamma(c-b)} {}_2\mathcal{F}_1(a, b, a+b-c+1; 1-z) \\ &+ (1-z)^{c-a-b} \frac{\Gamma(c)\Gamma(a+b-c)}{\Gamma(a)\Gamma(b)} {}_2\mathcal{F}_1(c-a, c-b, c-a-b+1; 1-z). \end{aligned} \quad |\arg(1-z)| < \pi \quad (66)$$

In general Gauss-Hypergeometric function,

$${}_2\mathcal{F}_1(a, b, c; z) = \sum_{n=0}^{\infty} \frac{(a)_n (b)_n}{(c)_n} \frac{z^n}{n!} \quad (67)$$

where  $(\cdot)_n$  denotes the Pochhammer symbol [64].

$${}_2\mathcal{F}_1(a, b, c; z) = 1 + \frac{ab}{c}z + \frac{a(a+1)b(b+1)}{c(c+1)} \frac{z^2}{2!} + \frac{a(a+1)(a+2)b(b+1)(b+2)}{c(c+1)(c+2)} \frac{z^3}{3!} + \dots \quad (68)$$

The series continues with additional terms involving higher powers of  $z$ . Each term in the series involves the parameters  $a$ ,  $b$ , and  $c$  as well as the variable  $z$  raised to a specific power.

Using the above relations eqs. (66) and (68), we approximate the Gauss-hypergeometric functions



$f_1$  and  $f_2$  present in the relation of the particle distribution function (see Eq.(59)) as follows:

$$\begin{aligned}
f_1 &= {}_2\mathcal{F}_1(1+a, 1+b; 1+c; y) \\
&= \frac{\Gamma(1+c)\Gamma(c-a-b-1)}{\Gamma(c-a)\Gamma(c-b)} {}_2\mathcal{F}_1(1+a, 1+b, 2+a+b-c; 1-y) \\
&+ \frac{\Gamma(1+c)\Gamma(1+a+b-c)}{\Gamma(1+a)\Gamma(1+b)} (1-y)^{(c-a-b-1)} {}_2\mathcal{F}_1(c-a, c-b, c-a-b; 1-y) \\
&= \left( \frac{c\Gamma(c)\Gamma(c-a-b-1)}{\Gamma(c-a)\Gamma(c-b)} \right) \left( 1 + \frac{(a+1)(b+1)}{(2+a+b-c)}(1-y) \right. \\
&+ \left. \frac{(a+1)(a+2)(b+1)(b+2)}{(2+a+b-c)(2+a+b-c+1)} \frac{(1-y)^2}{2!} + \dots \right) \\
&+ (1-y)^{(c-a-b-1)}(a+b-c) \left( \frac{c\Gamma(c)\Gamma(a+b-c)}{a\Gamma(a)b\Gamma(b)} \right) \left( 1 + \frac{(c-a)(c-b)}{(c-a-b)}(1-y) \right. \\
&+ \left. \frac{(c-a)(c-a+1)(c-b)(c-b+1)}{(c-a-b)(c-a-b+1)} \frac{(1-y)^2}{2!} + \dots \right) \tag{69}
\end{aligned}$$

Similarly,

$$\begin{aligned}
f_2 &= \frac{\Gamma(c)\Gamma(c-a-b)}{\Gamma(c-a)\Gamma(c-b)} {}_2\mathcal{F}_1(a, b, 1-c+a+b; 1-y) \\
&+ (1-y)^{(c-a-b)} \frac{\Gamma(c)\Gamma(a+b-c)}{\Gamma(a)\Gamma(b)} {}_2\mathcal{F}_1(c-a, c-b, 1+c-a-b; 1-y) \\
&= \frac{\Gamma(c)\Gamma(c-a-b)}{\Gamma(c-a)\Gamma(c-b)} \left( 1 + \frac{ab}{1+a+b-c}(1-y) + \frac{(a+1)(b+1)}{(2+a+b-c)} \frac{(1-y)^2}{2!} + \dots \right) \\
&+ (1-y)^{(c-a-b)} \frac{\Gamma(c)\Gamma(a+b-c)}{\Gamma(a)\Gamma(b)} \left( 1 + \frac{(c-a)(c-b)}{(1+c-a-b)}(1-y) + \dots \right) \tag{70}
\end{aligned}$$

Here,  $y$  is a variable that changes with time according to equation  $y = \frac{1}{2} \left( 1 + \tanh\left(\frac{t}{\tau}\right) \right)$ . As time progresses, especially in scenarios with significant time intervals like  $t > \tau$ , it becomes evident that  $(1-y)$  approaches zero. Consequently, the dominant impact on the particle distribution function in the limit  $y \rightarrow 1$  stemmed from the zeroth-order term independent of  $(1-y)$ . As discussed in many literature for deriving the asymptotic expression for the particle distribution function when  $y \simeq 1$ , the Gauss-hypergeometric functions  $f_1$  and  $f_2$  are truncated up to zeroth order only. [35, 60].

Building on the earlier discussion (see III A), our focus is primarily on understanding the dynamics of particle distribution function over finite time rather than just its asymptotic trends. We are examining  $f(\mathbf{p}, y)$  in the neighborhood of  $y = 1$ , keeping our investigation close to this limit. Suppose one wishes to analyze the finite-time behavior of the particle distribution function using expressions based on elementary functions. In that case, it is necessary to incorporate other higher-order terms in the expression of the particle distribution function. It means expanding the time-dependent particle distribution function as a power series in the small variable  $(1-y)$  as:

$$f(\mathbf{p}, y) \simeq C_0(\mathbf{p}, y) + (1-y)C_1(\mathbf{p}, y) + (1-y)^2C_2(\mathbf{p}, y) + \dots + (1-y)^nC_n(\mathbf{p}, y) \tag{71}$$

To compute an approximate expression for the particle distribution function depending on the finite time, we can truncate the power series of the Gauss-hypergeometric functions  $f_1$  and  $f_2$  that given by eqs. (69) and (70) up to a particular order. The specific order of truncation will depend on the accuracy required for analysis and the characteristics of the finite-time behavior in which we are interested.

Let's start by approximating the different terms present in the particle distribution relation (59):

$$\begin{aligned}
\frac{2}{\tau}y(1-y)\frac{ab}{c}f_1 &= \frac{2}{\tau}y\Gamma_1ab(1-y)\left(1+(1-y)\frac{(1+a)(1+b)}{(2+a+b-c)}\right) + \frac{2}{\tau}y\Gamma_2(a+b-c)(1-y)^{(c-a-b)} \\
&\quad \left(1+(1-y)\frac{(c-a)(c-b)}{(c-a-b)} + (1-y)^2\frac{(c-a)(c-b)(c-a+1)(c-b+1)}{(c-a-b)(c-a-b+1)}\right) \\
&= \frac{2}{\tau}y(a+b-c)\Gamma_2(1-y)^{(c-a-b)} + (1-y)\left(\frac{2}{\tau}yab\Gamma_1 - \frac{2y}{\tau}(c-a)(c-b)\Gamma_2(1-y)^{(c-a-b)}\right) \\
&\quad + (1-y)^2\left(\frac{2}{\tau}y\Gamma_1\frac{a(1+a)b(1+b)}{(2+a+b-c)} + \frac{2}{\tau}y\Gamma_2(1-y)^{(c-a-b)}\frac{(c-a)(c-b)(c-a+1)(c-b+1)}{(a+b-c-1)}\right)
\end{aligned} \tag{72}$$

where,  $\Gamma_1 = \frac{\Gamma(c)\Gamma(c-a-b-1)}{\Gamma(c-a)\Gamma(c-b)}$  and  $\Gamma_2 = \frac{\Gamma(c)\Gamma(a+b-c)}{\Gamma(a)\Gamma(b)}$ .

Similarly,

$$\begin{aligned}
(\omega(\mathbf{p}, y) - (1-y)\omega_0(\mathbf{p}) - y\omega_1(\mathbf{p}))f_2 &= (\omega(\mathbf{p}, y) - (1-y)\omega_0 - y\omega_1)\left(\Gamma_1(c-a-b-1)\right. \\
&\quad \left.(1+(1-y)\frac{ab}{(1+a+b-c)}) + (1-y)^{(c-a-b)}\Gamma_2\left(1+(1-y)\frac{(c-a)(c-b)}{(1+c-a-b)}\right)\right)
\end{aligned} \tag{73}$$

Also, it is possible to write down the time-dependent quasi-energy  $\omega(\mathbf{p}, y)$  as the following series expansion near  $y \rightarrow 1$  :

$$\omega(\mathbf{p}, y) = \omega_1 - \frac{2E_0\tau}{\omega_1}P_1(1-y) + \frac{2E_0^2\tau^2}{\omega_1^3}\epsilon_{\perp}^2(1-y)^2 \tag{74}$$

up to the second order and neglect the other higher order terms.

Therefore,

$$\begin{aligned}
(\omega(\mathbf{p}, y) - (1-y)\omega_0 - y\omega_1)f_2 &= (1-y)\left((\omega_1 - \omega_0) - \frac{2E_0\tau}{\omega_1}P_1\right)\left(\Gamma_1(c-a-b-1) + e^{-i\tau\omega_1 \ln(1-y)}\Gamma_2\right) \\
&\quad + (1-y)^2\left(\Gamma_1(c-a-b-1)\left(\frac{2E_0^2\tau^2\epsilon_{\perp}^2}{\omega_1^3} + \frac{ab(\omega_1(\omega_1 - \omega_0) - 2P_1E_0\tau)}{\omega_1(1+a+b-c)}\right)\right. \\
&\quad \left.+ \Gamma_2e^{-i\tau\omega_1 \ln(1-y)}\left(\frac{2E_0^2\tau^2\epsilon_{\perp}^2}{\omega_1^3} + \left((\omega_1 - \omega_0) - \frac{2E_0\tau}{\omega_1}P_1\right)\frac{(c-a)(c-b)}{(1+c-a-b)}\right)\right)
\end{aligned} \tag{75}$$

Using the above relation, we get

$$\begin{aligned}
& \left| \frac{2}{\tau} y(1-y) \frac{ab}{c} f_1 + i(\omega - (1-y)\omega_0 - y\omega_1) f_2 \right|^2 \\
& \simeq \left| \frac{2}{\tau} y(a+b-c) \Gamma_2 e^{-i\tau\omega_1 \ln(1-y)} + (1-y) \left[ \Gamma_1 \left( \frac{2}{\tau} yab + i(c-a-b-1)(\omega_1 - \omega_0 - \frac{2E_0\tau P_1}{\omega_1}) \right) \right. \right. \\
& \left. \left. + \Gamma_2 e^{-i\tau\omega_1 \ln(1-y)} \left( \frac{2}{\tau} y(a+b-c) \frac{(c-a)(c-b)}{(c-a-b)} + i(\omega_1 - \omega_0 - \frac{2E_0\tau P_1}{\omega_1}) \right) \right] + (1-y)^2 \left[ \Gamma_1 \left( \frac{2}{\tau} yab \right. \right. \right. \\
& \left. \left. \frac{(1+a)(1+b)}{(2+a+b-c)} + i \left( \frac{2E_0^2\tau^2\epsilon_\perp^2}{\omega_1^3} + \frac{ab}{(1+a+b-c)} (\omega_1 - \omega_0 - \frac{2E_0\tau P_1}{\omega_1}) \right) (c-a-b-1) \right) \right. \\
& \left. \left. + \Gamma_2 e^{-i\tau\omega_1 \ln(1-y)} \left( \frac{2}{\tau} y(a+b-c) \frac{(c-a)(c-b)(c-a+1)(c-b+1)}{(c-a-b)(c-a-b+1)} + \frac{2E_0^2\tau^2\epsilon_\perp^2}{\omega_1^3} \right. \right. \right. \\
& \left. \left. \left. + (\omega_1 - \omega_0 - \frac{2E_0\tau P_1}{\omega_1}) \frac{(c-a)(c-b)}{(1+c-a-b)} \right) \right] \right|^2 \quad (76)
\end{aligned}$$

We introduce it here in anticipation of encountering the Gamma function  $\Gamma(z)$  in the subsequent content. The Gamma function typically obeys the following relationship:

$$\Gamma(1+z) = z\Gamma(z), \quad \Gamma(1-z)\Gamma(z) = \frac{\pi}{\sin(\pi z)}, \quad (77)$$

from which we can derive the following useful relations,

$$|\Gamma(iz)|^2 = \frac{\pi}{z \sinh(\pi z)}, \quad |\Gamma(1+iz)|^2 = \frac{\pi z}{\sinh(\pi z)}, \quad \left| \Gamma\left(\frac{1}{2} + iz\right) \right|^2 = \frac{\pi}{\cosh(\pi z)} \quad (78)$$

Using the mathematical identities (78), we can compute  $|\Gamma_1|^2$  and  $|\Gamma_2|^2$  as

$$\begin{aligned}
|\Gamma_1|^2 &= \left| \frac{\Gamma(c)\Gamma(c-a-b-1)}{\Gamma(c-a)\Gamma(c-b)} \right|^2 \\
&= \frac{\omega_0(\omega_1 + \omega_0 + 2E_0\tau)}{\omega_1(\omega_1 + \omega_0 - 2E_0\tau)(1 + \tau^2\omega_1^2)} \left( \frac{\sinh(\frac{\pi\tau}{2}(\omega_0 + \omega_1 - 2E_0\tau)) \sinh(\frac{\pi\tau}{2}(\omega_0 + \omega_1 + 2E_0\tau))}{\sinh(\pi\tau\omega_0) \sinh(\pi\tau\omega_1)} \right) \\
|\Gamma_2|^2 &= \left| \frac{\Gamma(c)\Gamma(a+b-c)}{\Gamma(a)\Gamma(b)} \right|^2 \\
&= \frac{\omega_0(\omega_0 - \omega_1 + 2E_0\tau)}{\omega_1(\omega_1 - \omega_0 + 2E_0\tau)(1 + \tau^2\omega_1^2)} \left( \frac{\sinh(\frac{\pi\tau}{2}(\omega_0 - \omega_1 + 2E_0\tau)) \sinh(\frac{\pi\tau}{2}(-\omega_0 + \omega_1 + 2E_0\tau))}{\sinh(\pi\tau\omega_0) \sinh(\pi\tau\omega_1)} \right) \quad (79)
\end{aligned}$$

When computing expressions like  $\Gamma_1\bar{\Gamma}_2$ , approximate methods prove advantageous. A frequently utilized technique entails utilizing Stirling's formula for the Gamma function, offering a simpler yet effective approach to assess the desired expression.

$$\Gamma(z) \approx z^{z-1/2} e^{-z} \sqrt{2\pi} \quad (80)$$

Then, we derive the set of equations employing Stirling's formula for the Gamma function, which are used to determine the Gamma function in the computation of the particle distribution function.

$$\begin{aligned}\Gamma(1 + ix) &\sim \sqrt{2\pi}e^{(\frac{1}{2}\ln(x) - \frac{\pi}{2}x) + i(x(\ln(x)-1) + \frac{\pi}{4})} \\ \Gamma(-ix) &\sim \sqrt{2\pi}e^{(\frac{\pi}{2}x - \frac{1}{2}\ln(x)) + i(x(1 - \ln(x)) - \frac{\pi}{4})} \\ \Gamma(ix) &\sim \sqrt{2\pi}e^{(-\frac{\pi}{2}x - \frac{1}{2}\ln(x)) + i(x(\ln(x)-1) - \frac{\pi}{4})}\end{aligned}\quad (81)$$

So,

$$\Gamma_1 \bar{\Gamma}_2 = \left( \frac{\Gamma(c)\Gamma(c-a-b-1)}{\Gamma(c-a)\Gamma(c-b)} \right) \overline{\left( \frac{\Gamma(c)\Gamma(a+b-c)}{\Gamma(a)\Gamma(b)} \right)} \quad (82)$$

Subsequently, following certain algebraic manipulations, we obtain :

$$\Gamma_1 \bar{\Gamma}_2 = |\Gamma_1 \bar{\Gamma}_2| e^{i\varrho} \quad (83)$$

where,

$$|\Gamma_1 \bar{\Gamma}_2| = \frac{\omega_0}{2\omega_1} \frac{\exp(\pi\tau/2(\omega_0 - \omega_1 + 2E_0\tau))}{\sinh(\pi\tau\omega_0) \sqrt{1 + \omega_1^2\tau^2}} \sqrt{\frac{((\omega_0 + 2E_0\tau)^2 - \omega_1^2)}{(\omega_1^2 - (2E_0\tau - \omega_0)^2)}} \quad (84)$$

$$\begin{aligned}\varrho &= \frac{\tau}{2}(\omega_0 + \omega_1 - 2E_0\tau) \ln(\tau(\omega_0 + \omega_1 - 2E_0\tau)) + (-\omega_0 + \omega_1 - 2E_0\tau) \ln(\tau(\omega_0 - \omega_1 + 2E_0\tau)) \\ &+ (-\omega_0 + \omega_1 + 2E_0\tau) \ln(\tau(-\omega_0 + \omega_1 + 2E_0\tau)) + (\omega_0 + \omega_1 + 2E_0\tau) \ln(\tau(\omega_0 + \omega_1 + 2E_0\tau)) \\ &+ \pi - \tan^{-1}(\tau\omega_1) - 2\tau\omega_1 \ln(2\omega_1\tau)\end{aligned}\quad (85)$$

Now, we use these approximations of the Gamma function to derive an approximate expression for the particle distribution function (59), which can then be re-expressed using Eq.(76) as follows:

$$\begin{aligned}f(\mathbf{p}, y) &\simeq |N^+(\mathbf{p})|^2 \left[ \frac{2}{\tau} y(a+b-c) \Gamma_2 e^{-i\tau\omega_1 \ln(1-y)} + (1-y) \left[ \Gamma_1 \left( \frac{2}{\tau} yab + i(c-a-b-1)(\omega_1 - \omega_0 - \frac{2E_0\tau P_1}{\omega_1}) \right) \right. \right. \\ &+ \Gamma_2 e^{-i\tau\omega_1 \ln(1-y)} \left( \frac{2}{\tau} y(a+b-c) \frac{(c-a)(c-b)}{(c-a-b)} + i(\omega_1 - \omega_0 - \frac{2E_0\tau P_1}{\omega_1}) \right) \left. \right] + (1-y)^2 \left[ \Gamma_1 \left( \frac{2}{\tau} yab \right. \right. \\ &\left. \left. \frac{(1+a)(1+b)}{(2+a+b-c)} + i \left( \frac{2E_0^2\tau^2\epsilon_{\perp}^2}{\omega_1^3} + \frac{ab}{(1+a+b-c)} (\omega_1 - \omega_0 - \frac{2E_0\tau P_1}{\omega_1}) \right) (c-a-b-1) \right) \right. \\ &+ \Gamma_2 e^{-i\tau\omega_1 \ln(1-y)} \left( \frac{2}{\tau} y(a+b-c) \frac{(c-a)(c-b)(c-a+1)(c-b+1)}{(c-a-b)(c-a-b+1)} + \frac{2E_0^2\tau^2\epsilon_{\perp}^2}{\omega_1^3} \right. \\ &\left. \left. + (\omega_1 - \omega_0 - \frac{2E_0\tau P_1}{\omega_1}) \frac{(c-a)(c-b)}{(1+c-a-b)} \right) \right] \left| \left( 1 + \frac{P(p_{\parallel}, y)}{\omega(\mathbf{p}, y)} \right) \right|^2\end{aligned}\quad (86)$$

To explore the behavior of the particle distribution function at finite times ( $t > \tau$ ), we aim to express  $f(\mathbf{p}, y)$  in a series involving  $(1 - y)$ , as discussed previously (refer to Eq. (71)). We can then consider truncating higher-order terms to simplify the analysis while still capturing essential features. In this context, we focus exclusively on terms up to the  $(1 - y)^2$  order, disregarding higher-order terms in Eq. (86). This approach is sufficient to explain the interesting results discussed in the later section IV. To accomplish this, we again approximate the quantity  $\left(1 + \frac{P(\mathbf{p}, y)}{\omega(\mathbf{p}, y)}\right)$  using the Taylor series expansion near  $y \rightarrow 1$ . This yields:

$$1 + \frac{P(\mathbf{p}, y)}{\omega(\mathbf{p}, y)} = \Omega_0 + \Omega_1(1 - y) + \Omega_2(1 - y)^2 \quad (87)$$

up to second order and neglect the other higher order terms. with,

$$\Omega_0 = 1 + \frac{P_1}{\omega_1}; \quad (88)$$

$$\Omega_1 = \frac{-2E_0\tau}{\omega_1^3} \epsilon_{\perp}^2; \quad (89)$$

$$\Omega_2 = \frac{-6E_0^2\tau^2}{\omega_1^5} P_1 \epsilon_{\perp}^2. \quad (90)$$

After extensive calculations, we can derive an approximate expression for the particle distribution function in terms of the small parameter  $(1 - y)$  up to the second order. This expression is given by:

$$f(\mathbf{p}, y) \approx |N^+(\mathbf{p})|^2 \left( C_0(\mathbf{p}, y) + (1 - y)C_1(\mathbf{p}, y) + (1 - y)^2 C_2(\mathbf{p}, y) \right) \quad (91)$$

where,

$$C_0(\mathbf{p}, y) = 4y^2 \Omega_0 \omega_1^2 |\Gamma_2|^2 \quad (92)$$

$$C_1(\mathbf{p}, y) = 4y \Omega_0 |\Gamma_1 \overline{\Gamma_2}| E_0 \tau (P_1 - \omega_1) \cos(\Upsilon) + 4y |\Gamma_2|^2 (2\Omega_0 (\omega_1^2 - \omega_0 \omega_1 + (\omega_1 - P_1) E_0 \tau) + \Omega_1 \omega_1^2 y) \quad (93)$$

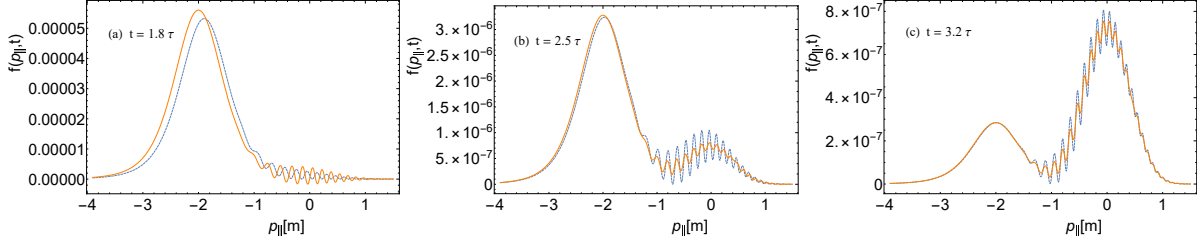


Figure 2: Particle momentum distribution function,  $f(p_{\parallel}, p_{\perp} = 0, t)$  for different times with the laser field parameter  $E_0 = 0.2E_c$  and  $\tau = 10[m^{-1}]$ . Here, the dashed blue line represents the exact result, while the solid orange line is from the approximate calculation and all the units are taken in electron mass unit.

$$\begin{aligned}
C_2(\mathbf{p}, y) = & \Omega_0(P_1 - \omega_1)^2 \frac{4E_0^2 \tau^2}{\omega_1^2} |\Gamma_1|^2 + |\Gamma_2|^2 \left[ 8\Omega_1 y (2E_0 \tau (\omega_1 - P_1) - \omega_0 \omega_1 + \omega_1^2) - 8\Omega_0 y (\omega_1 + P_1) \right. \\
& (\omega_1 - \omega_0 + 2E_0 \tau) + 4\Omega_2 y^2 \omega_1^2 + \Omega_0 \left( \frac{4}{\omega_1^2} (\omega_1^2 + E_0 \tau (\omega_1 - P_1))^2 + \frac{\tau^2}{4} ((\omega_0 + \omega_1)^2 - 4E_0^2 \tau^2)^2 y^2 \right) \\
& + \frac{y \Omega_0}{2\omega_1^2 (1 + \tau^2 \omega_1^2)} \left( 2\omega_1^2 \tau^2 ((\omega_0 - \omega_1) \omega_1 + 2E_0 \tau P_1) (\omega_0^2 - (\omega_1 + 2E_0 \tau)^2) \right. \\
& + y \omega_1^3 (16(\omega_0 + \omega_1) + 32E_0 \tau - 4(2\omega_0 - 3\omega_1)(\omega_0 + \omega_1)^2 \tau^2 + 8E_0 \tau^3 \omega_1 (2\omega_0 + 3\omega_1) \\
& - \tau^4 (\omega_1 (\omega_0 + \omega_1)^4 - 16E_0^2 (2\omega_0 + \omega_1)) + 32E_0^3 \tau^5 + 8E_0^2 \tau^6 \omega_1 (\omega_0 + \omega_1)^2 - 16E_0^4 \tau^8 \omega_1) \\
& \left. + 16E_0^2 \tau^2 \epsilon_{\perp}^2 (1 + \tau^2 \omega_1^2) \right] + \frac{|\Gamma_1 \bar{\Gamma}_2| \cos(\Upsilon)}{2\omega_1^2 (4 + \omega_1^2 \tau^2)} \left( -16E_0^4 \Omega_0 \omega_1^4 \tau^8 y^2 \right. \\
& + 16E_0^3 \Omega_0 \omega_1^2 \tau^5 y (P_1 (4 + \omega_1^2 \tau^2) - 4\omega_1 y) + \Omega_0 \omega_1^2 (-\omega_0 + \omega_1) y (2(-8(\omega_1 + P_1) \\
& + (\omega_0 - \omega_1)^2 \omega_1 \tau^2) (4 + \omega_1^2 \tau^2) + \omega_1 (32 - 4(\omega_0 - \omega_1)(4\omega_0 + \omega_1) \tau^2 + (\omega_0 - \omega_1)^3 \omega_1 \tau^4) y) \\
& + 8E_0^2 \Omega_0 \tau^2 (-2(\omega_1 - P_1)^2 (4 + \omega_1^2 \tau^2) - (4 + \omega_1^2 \tau^2) (-2P_1^2 + \omega_1^2 (2 + \omega_1 (-\omega_0 + \omega_1) \tau^2))) y \\
& + \omega_1^3 \tau^2 (-8\omega_0 + 6\omega_1 + (\omega_0 - \omega_1)^2 \omega_1 \tau^2) y^2 + 4E_0 \omega_1^2 \tau (-4\Omega_0 (\omega_1 - P_1) (4 + \omega_1^2 \tau^2) \\
& - (4 + \omega_1^2 \tau^2) (4\Omega_1 (\omega_1 - P_1) - 8\Omega_0 (\omega_1 + P_1) + \Omega_0 (\omega_0 - \omega_1)^2 P_1 \tau^2) y \\
& \left. - 4\Omega_0 \omega_1 (4 + (-\omega_0^2 + \omega_1^2) \tau^2) y^2 \right) + \frac{|\Gamma_1 \bar{\Gamma}_2| \Omega_0 \tau y}{(\omega_1 (4 + \omega_1^2 \tau^2))} \left( 2(4 + \omega_1^2 \tau^2) (\omega_1^3 (2 + \omega_1) \right. \\
& - E_0 \omega_1^2 (\omega_1 + 3P_1) \tau + 4E_0^2 (\omega_1^2 + \omega_1 (-2 + P_1) - P_1^2) \tau^2 + 4E_0^3 (-\omega_1 + P_1) \tau^3) \\
& + \omega_0^4 \omega_1^2 \tau^2 y - \omega_1^2 (\omega_1 - 2E_0 \tau) (12\omega_1 + 8E_0 \tau + 3\omega_1^3 \tau^2 + 2E_0 \omega_1^2 \tau^3 - 4E_0^2 \omega_1 \tau^4 + 8E_0^3 \tau^5) y \\
& + 4\omega_0 \omega_1^2 (4 + \omega_1^2 \tau^2) (-2 + \omega_1 y) + 2\omega_0^2 ((\omega_1 (2 + \omega_1) + E_0 (\omega_1 - P_1) \tau) (4 + \omega_1^2 \tau^2) \\
& \left. - y \omega_1^2 (10 + 3\omega_1^2 \tau^2 - 2E_0 \omega_1 \tau^3 + 4E_0^2 \tau^4)) \right) \sin(\Upsilon) \tag{94}
\end{aligned}$$

Here,  $\Upsilon = \varrho + \tau \omega_1 \ln(1 - y)$ . and also note that  $C_0$ ,  $C_1$ , and  $C_2$  are independent of the function of  $(1 - y)$ .

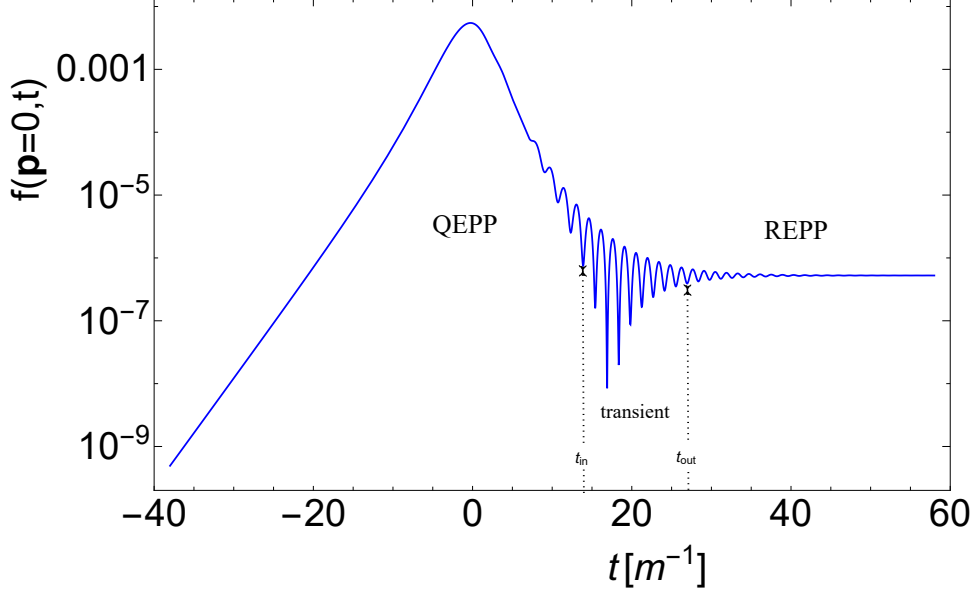


Figure 3: Time evolution of  $\mathbf{f}(\mathbf{p}, t)$  with  $E_0 = 0.2E_c$  and  $\tau = 10[m^{-1}]$  and all the units are taken in electron mass unit.

To verify the accuracy of the approximate expression (91), we will directly compare it with the exact relation (59). For this purpose, we plot the approximate relation (91) against the exact one for  $t > \tau$ , as shown in Fig.2. This comparison is crucial for analytically investigating the momentum spectra of created particles at finite time (see Sect. IV B 1). In Fig. 2(a), we observe a small discrepancy between the exact and approximate results that appear to depend on  $t$ . Consequently, the approximate result provides a very accurate prediction for  $t \geq 2\tau$ , as shown in Fig. 2. Upon evaluating Eq. (91), we obtain  $f(p_{\parallel} = 0, t) \approx 7.97 \times 10^{-7}$ . The mean relative error of the approximate result is below 0.2% at time  $t = 2.5\tau$  (see Fig. 2(b)). As time progresses, both approaches give nearly the same result, as illustrated in Fig. 2(c) at  $t = 3\tau$ . Based on the relation (91), we will discuss the analysis of the approximate momentum distribution function for longitudinal and transverse momentum, expressed in terms of elementary functions (see sections IV B and IV E). This characteristic makes this case especially convenient for physical interpretations.

## IV. RESULTS AND DISCUSSION

### A. Temporal evolution of particle distribution

Quantum vacuum becomes unstable under the action of the external electric field. As a consequence, virtual particle-antiparticle pairs are created in an off-mass-shell configuration. These vir-

tual charged particles are accelerated by the electric field to enough energy to become real particles in an on-shell mass configuration. During the action of the external force, pair annihilation processes occur simultaneously with the pair creation, giving rise to a dynamical quasiparticle plasma. This results in different states of in and out-vacuum. The most complete description of vacuum pair creation from in-state to out-state is given by the one-particle distribution function. The time evolution of the one-particle distribution function shows that virtual particle-antiparticle (electron-positron plasma(EPP)) excited from vacuum passes through three different temporal stages: the quasiparticle electron-positron plasma (QEPP) stage, the transient stage, and the final residual electron-positron plasma(REPP) in the out-state as pointed by authors of [65] see figure 3. The initial stage QEPP and the final REPP stage are separated by the fast oscillation of EPP by the transient stage. The transient stage is considered to begin at time  $t_{in}$  where oscillating of  $f(t)$  attains the REPP level for the first time. The time  $t_{out}$  where the transient stage ends is taken as the time when the average level of the oscillating  $f(t)$  hits the REPP; after that, the REPP stage begins. At the REPP stage, quasi-particles become independent, and real particle-antiparticles are observed with a lesser value off than that at the electric field maximum at  $t = 0$ .

Each of the three stages contributes to the various physical effects, such as vacuum polarization effects [70], the emission of annihilation photons originating from the focal point of colliding laser beams [65, 71–73], the birefringence effect [74], and various other secondary effects. In order to estimate the contributions of the various stages in measuring observable effects, a detailed analysis of each period of the EPP's evolution is quite helpful.

Since the particle distribution function depends on the kinetic momentum  $p_{\parallel} = p_3$  parallel to the direction of the electric field and the modulus of the transverse momentum  $p_{\perp} = \sqrt{p_1^2 + p_2^2}$ . Due to the rotation symmetry of the problem about the field axis, one may parameterize the kinetic momentum vector as  $\mathbf{p} = (p_1, 0, p_3)$  with the transverse component,  $p_{\perp} = p_1$  and longitudinal component  $p_{\parallel} = p_3$ .

In Fig. 4 illustrates how the temporal evolution of quasi-particle distribution functions  $f(\mathbf{p}, t)$  depends on the momentum. As depicted in the left panel of Fig. 4, the particle distribution function  $f(p_{\parallel}, t)$  demonstrates a consistent increase over time within the region of QEPP. Notably, it shows a higher value for negative longitudinal momentum value than positive ones. On closer inspection, it becomes evident that the distribution function reaches its peak precisely when the longitudinal quasi-momentum,  $P(t) \simeq 0$ . This particular peak occurrence is influenced by the specific choice of  $p_{\parallel}$  value. After  $t = 0[m^{-1}]$ , where the electric field reaches its maximum value,  $f(p_{\parallel}, t)$  decreases.  $f(p_{\parallel}, t)$ , after decreasing to a certain value, shows rapid oscillations and thus



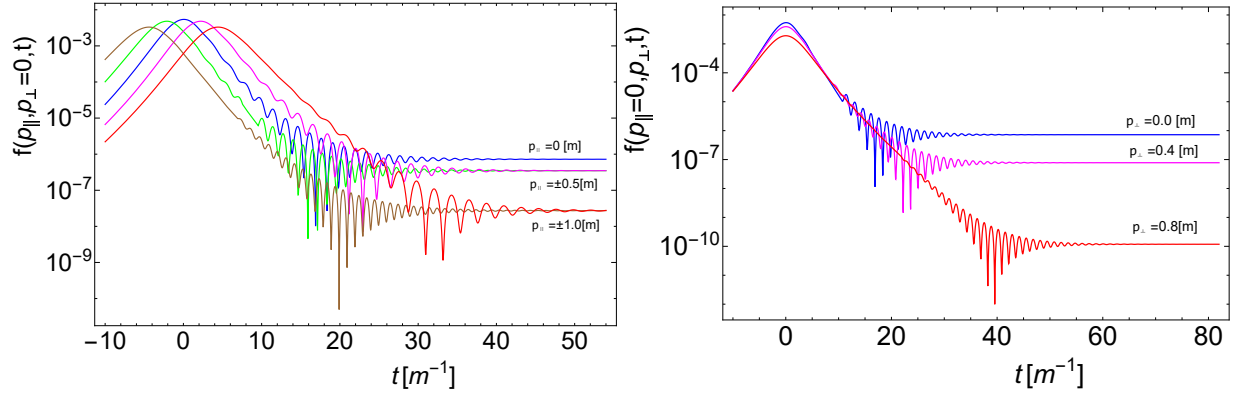


Figure 4: The relationship between momentum and the transient domain's time of occurrence. **Left panel:** for longitudinal momentum **Right panel:** for transverse momentum with  $E_0 = 0.2E_c$  and  $\tau = 10[m^{-1}]$  and all the units are taken in electron mass unit.

transitions from QEPP to a transient region.

$p_{\parallel}[m]$	$t_{in}[m^{-1}]$	$f(p_{\parallel}, t_{in})$	$t_{out}[m^{-1}]$	$f(p_{\parallel}, t_{out})$
0.0	12.57	$7.203 \times 10^{-7}$	24.038	$3.309 \times 10^{-7}$
0.25	13.37	$5.576 \times 10^{-7}$	24.803	$3.112 \times 10^{-7}$
0.50	13.78	$2.242 \times 10^{-7}$	24.320	$1.599 \times 10^{-7}$
0.75	14.53	$7.769 \times 10^{-8}$	25.799	$7.033 \times 10^{-8}$
1.00	16.76	$1.748 \times 10^{-8}$	26.866	$1.082 \times 10^{-8}$

Table I: Transient region time labeled by longitudinal momentum  $p_{\parallel}$ . The time interval during which a strong oscillation emerges in the evolution of the distribution function is referred to as  $t_{in}$ , and  $t_{out}$  marks the point where this vigorous oscillation diminishes, leading to a residual distribution function. The value of transverse momentum is taken to be zero and all the units are taken in electron mass unit. The field parameters are  $E_0 = 0.2E_c$  and  $\tau = 10[m^{-1}]$ .

One observes a gradual narrowing and a disappearance of the fluctuations in the transient domain for higher  $p_{\parallel}$ - value. The transient region appears later for a higher  $p_{\parallel}$ - value. We confirm this by quantifying the period of the transient stage,  $t_{in}$  and  $t_{out}$  as shown in Table 1. The transient stage starts nearly after  $t \approx \tau$  (see Table 1). After that, it reaches the REPP stage, where the distribution function,  $f_{out}$ , becomes constant.  $f_{out}$  being largest for  $p_{\parallel} = 0$  and the same for positive and negative  $p_{\parallel}$ - value.

Next, we point out the influence of transverse momentum on temporal stages, as seen from the right panel of Fig. 4. We can observe an interesting behavior for the higher transverse momentum

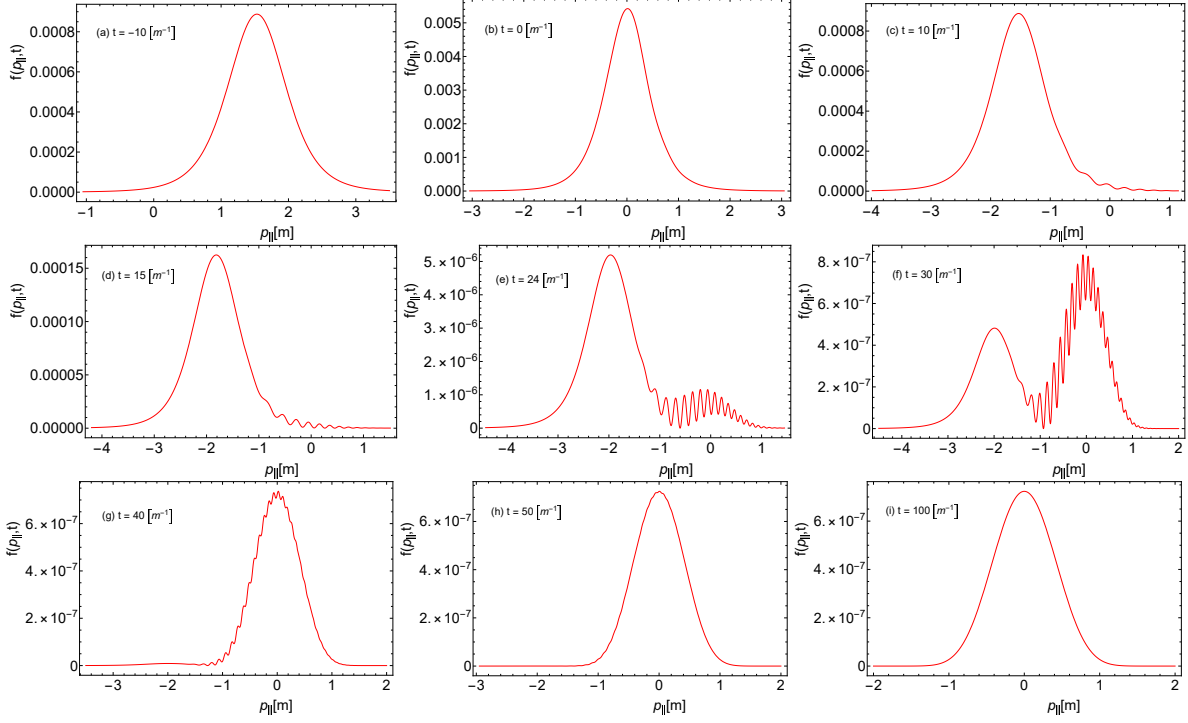


Figure 5: Time evolution of particle distribution function in the momentum space  $f(p_{\parallel}, t)$  at different times. The transverse momentum is considered to be zero, and all the units are taken in the electron mass unit. The field parameters are  $E_0 = 0.2E_c$  and  $\tau = 10[m^{-1}]$ .

value,  $f(p_{\perp})$  slowly reaches to REPP stage with the residual value  $f(p_{\perp}, t > t_{out})$  which is lowest in comparison to small transverse momentum value  $p_{\perp}$ . These stages behaviors are mainly decided by the double quasi-energy  $2\omega(p_{\parallel}, p_{\perp}, t)$ , as we increase the transverse momentum corresponding transverse energy  $\epsilon_{\perp}(p_{\perp})$  also increases that come in the dynamical energy gap  $2\omega(p_{\parallel}, p_{\perp}, t)$  and due to which to reach on-shell condition (REPP stage) takes a longer time.

## B. Longitudinal Momentum Spectrum

In this section, we discuss about longitudinal momentum spectrum (LMS) of the created particle.

From figure 5, we see how particle creation proceeds. At early times,  $t = -10[m^{-1}]$  in the QEPP region when the electric field is increasing, the created particle shows a smooth Gaussian-like structure of momentum spectrum with a peak around  $p_{\parallel} \approx 2[m]$ . The electric field propels the newly created particles towards the negative  $z$ -direction. The movement of the distribution function's peak from  $p_{\parallel} = +2$  ( $+eE_0\tau$ ) to  $-2$  ( $-eE_0\tau$ ) can be understood through the concept of

quasi-momentum  $P(t) = (p_{\parallel} - eA(t))$ , as depicted in the time evolution shown in Figure 5(a) to (c). This phenomenon implies that the momentum distribution of the generated particles is expected to be distributed over a range of  $\Delta p_{\parallel} = 2$ , a spread determined by the electric field's magnitude. At time  $t = 0[m^{-1}]$  where the electric field is maximum ( $E(t) = E_0$ ), magnitude of longitudinal momentum distribution function  $f(p_{\parallel} = 0, t = 0) \approx 5 \times 10^{-3}$  that follows the tendency  $E^2(t)/8$  [75]. For  $t > 0$ , when there's a decrease in the strength of the field, an interesting phenomenon occurs in the momentum distribution function  $f(p_{\parallel})$ . It rapidly drops to 99.2% of its maximum value, driven by its reliance on the strength of the electric field at  $t = 10[m^{-1}]$ , as illustrated in figure 5(c). The  $f(p_{\parallel})$  peak corresponds to newly generated particles. However, within a narrow range of  $-1 < p_{\parallel} < 1$ , during what we term the transient stage, the typically smooth Gaussian shape of the distribution is disrupted. This disruption coincides with a weakening of the accelerating field's effect, which can be visualized in figure 5(d). Near  $t \approx 2\tau$ , when the electric field's magnitude dwindles to roughly 93% of its maximum, a secondary peak emerges within the LMS. This peak manifests around a longitudinal momentum value of zero, accompanied by observable oscillations within a confined range of  $p_{\parallel}$ , as demonstrated in figure 5(e). In proximity to  $p_{\parallel} = 0$ , this secondary peak experiences growth over time as the electric field weakens, while concurrently, the dominant peak begins to diminish. At  $t = 3\tau$ , we see that the small peak is now the dominant peak and shows oscillatory behavior near the transient stage and at the beginning of the REPP stage, as we see in figure 5(f) that oscillatory behavior in a small window of longitudinal momentum where the electric field diminishes to around one-hundredth of its maximum magnitude. Intriguingly, this oscillation exhibits an asymmetry, with its amplitude being more pronounced for negative longitudinal momentum compared to its positive longitudinal momentum. Within figure 5(f), the Gaussian bump centered around  $p_{\parallel} \approx -2[m]$  arises from particles generated during the initial phases of the process. Conversely, the dominant peak, characterized by the initiation of oscillation, comprises particles formed at later instances, which have encountered relatively less acceleration since their inception. This oscillation in the LMS finds its origin in the quantum interference effect, a phenomenon stemming from the outcomes of dynamical tunneling, as elucidated in reference [76]. Around  $t \approx 4\tau$ , a minor peak at  $p_{\parallel} = -2[m]$  value is nearly diminished. Only the dominant peak at  $p_{\parallel} = 0$  persists, with a faint onset of oscillatory behavior superimposed on a Gaussian-like structure eventually, as depicted in figures 5(g) to (h), the oscillation gradually fades away by  $t = 50[m^{-1}]$ . Dynamical tunneling can be grasped as a process evolving over time involving inter-band dynamics in particle momentum representation[77]. Within momentum space, various channels offer possibilities for particle tunneling. As time advances, distinct scenarios emerge: (i) At the time  $t$ , a particle

can tunnel directly, adopting a momentum value denoted as  $p'_{\parallel}$ , (ii) In the early stages, a particle exhibiting lower momentum ( $p_{\parallel} < p'_{\parallel}$ ) can tunnel, followed by acceleration leading to momentum  $p'_{\parallel}$ , (iii) Conversely, a particle initially possessing higher momentum ( $p_{\parallel} > p'_{\parallel}$ ) can tunnel at time  $t_1$  and subsequently decelerate to reach the specific momentum  $p'_{\parallel}$ . Finally, when the individual probability amplitudes of this process are added together, they result in quantum interference at time  $t$ . At the asymptotic time, those processes do not share the same phase information and become random due to averaging over particle paths that do not show quantum interference effects, which leads to a smooth distribution function. Many research articles, including the work by Dumlu et al. [78] have pointed out that LMS doesn't exhibit an oscillatory structure for the Sauter pulsed field as time approaches infinity. Instead, it displays a single-peaked Gaussian-like structure. This observation is consistent with the outcome illustrated in figure 5(i) at  $t = 100[m^{-1}]$ .

Certainly, we can establish certain time scales linked to the quantum signature manifesting as oscillations within the LMS of created particles. Drawing from the emergence of a secondary peak, we define three distinct time scales: (i)  $t_{cp}$  (Central Peak Formation): This time scale is characterized by the emergence of the secondary peak and the beginning of its development, (ii)  $t_{sep}$  (Peak Separation): At this time, the central peak becomes dominant or the time after the two peaks become distinctly separated, (iii)  $t_{dis}$  (Disappearance of Oscillation): This indicates the time when the oscillations within the central peak fade away or the time after the primary peak (or the left-side peak) ceases to exist. By identifying and quantifying these time scales, we can better characterize the intricate quantum dynamics reflected in the LMS during the REPP stage. Furthermore, it's

$E_0[E_c]$	$t_{cp}[m^{-1}]$	$t_{sep}[m^{-1}]$	$t_{dis}[m^{-1}]$
0.1	47	57	70
0.2	22	30	50
0.3	15	20	35
0.4	9	15	28
0.5	6	12	23

Table II: The effect of electric field strength  $E_0$  on time scale related to the formation of a central peak. The time scale  $t_{cp}$  appearance of a central peak,  $t_{sep}[m^{-1}]$  when two peaks become distinctly separated, and  $t_{dis}$  disappearance of the oscillation in LMS.

important to highlight that these time scales are influenced by the electric field strength  $E_0$ , as indicated in Table 2. A remarkable pattern becomes apparent upon examining the table—a consistent behavior of these three-time scales emerges with an increase in  $E_0$ . Additionally, there is a clear

trend where these events tend to occur earlier in time as  $E_0$  increases.

Moreover, our observations extend to the spread of  $\Delta p$  within the LMS, which exhibits changes depending on the value of  $E_0$ . This relationship is intuitively valid, as higher values of  $E_0$  correspond to greater kinetic momentum.

During the acceleration of the quasi-particle, we see the first Gaussian peak shift to the negative z-direction, and deformation in the tail gives the second peak in the spectrum around  $t = 2.3\tau$  that is clearly visible with interference visibility of 0.5. There are two distinct peaks here: one shows the smooth Gaussian-like structure, and the other shows the interference with effect as an oscillation at time  $t = 2.65\tau$  with visibility (or degree of coherence) of 0.314. The Gaussian-like onset oscillation peak is then dominated by  $t = 3\tau$ , reducing visibility to 0.15. This oscillation was observed in the Gaussian-like structure, which fades at  $t = 3.34\tau$  and has a visibility of 0.08. From these, we can say that these oscillations are seen in LMS at the Compton time scale during the formation of electrons or positrons. The LMS figure shows that coherence abruptly disappears at  $t = 4.15\tau$ , where visibility is 0.02.

We still do not talk about the Keldysh parameter,  $\gamma$ , on which we categorize the pair production process, whether it is governed by multi-photon or tunneling mechanisms. We also test whether this oscillation structure behavior explicitly depends on  $\gamma$  or not. We choose the  $\gamma$  value using two different combinations of  $E_0$  and  $\tau$  to see its behavior at a finite time. To show that the same value of Keldysh parameter,  $\gamma$ , gives a different qualitative picture of LMS at a finite time, here we take  $\gamma = 1$  corresponding to two different configurations of parameter  $(E_0, \tau)$  related to Sauter pulse electric field. As we know that  $\gamma = 1$  gives an intermediate regime of pair production via tunneling and multi-photon processes, which are known as the nonperturbative [79]. Fig. 6 shows LMS for Sauter pulse electric field with  $E_0 = 0.2$  and  $\tau = 5[m^{-1}]$ . From fig. 6 (a) to 6(c) we can see that due to the electric field smooth uni-modal Gaussian structure accelerated towards negative z-direction and after the pulse duration  $t = 6[m^{-1}]$  we observed some disturbance near the  $p_{\parallel} = 1$ . At  $t = 11.5[m^{-1}]$  interference effect is observed due to which smooth Gaussian structure becomes a multi-modal structure as shown in figure 6(d) and 6(e). That interference effect nearly disappear at  $t \approx 4\tau$ . Comparing figures 7(d) and 7(e), distinct structural differences become evident. These disparities contribute to the presence of two qualitatively distinct behaviors at finite times, both under the condition of  $\gamma = 1$ .

It's important to emphasize that this behavior during finite times is primarily influenced by the width of the pulse  $\tau$ . Depending on the classification of short and long pulses, we can outline two distinct behaviors: (i) Long Pulse Behavior ( $\tau > 8$ ): In this regime, two Gaussian-pulse

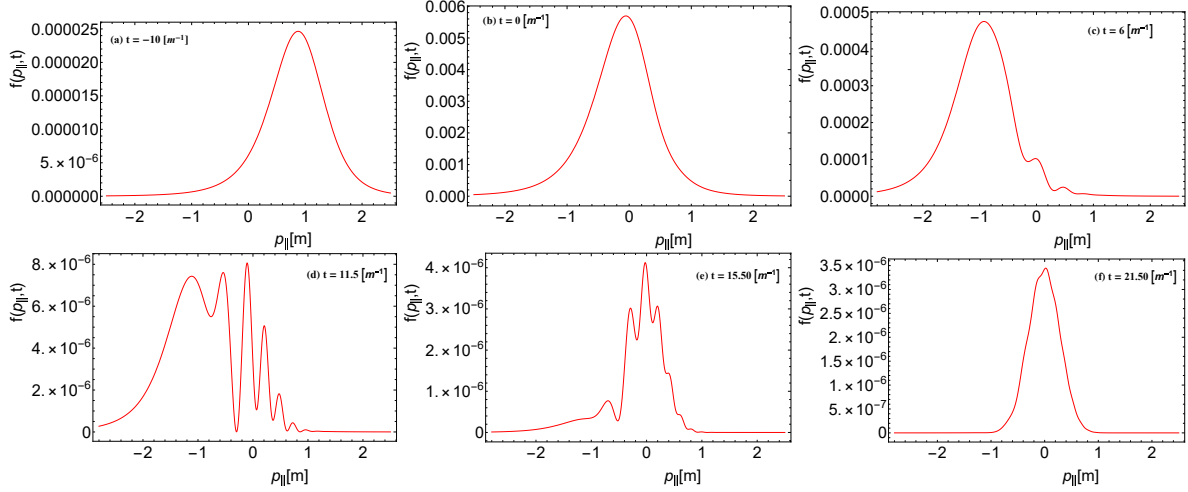


Figure 6: Time evolution of quasi-particle distribution function in the longitudinal momentum space  $f(p_{\parallel}, t)$ . The transverse momentum is considered to be zero and all the units are taken in the electron mass unit. The field parameters are  $E_0 = 0.2E_c$  and  $\tau = 5[m^{-1}]$ .

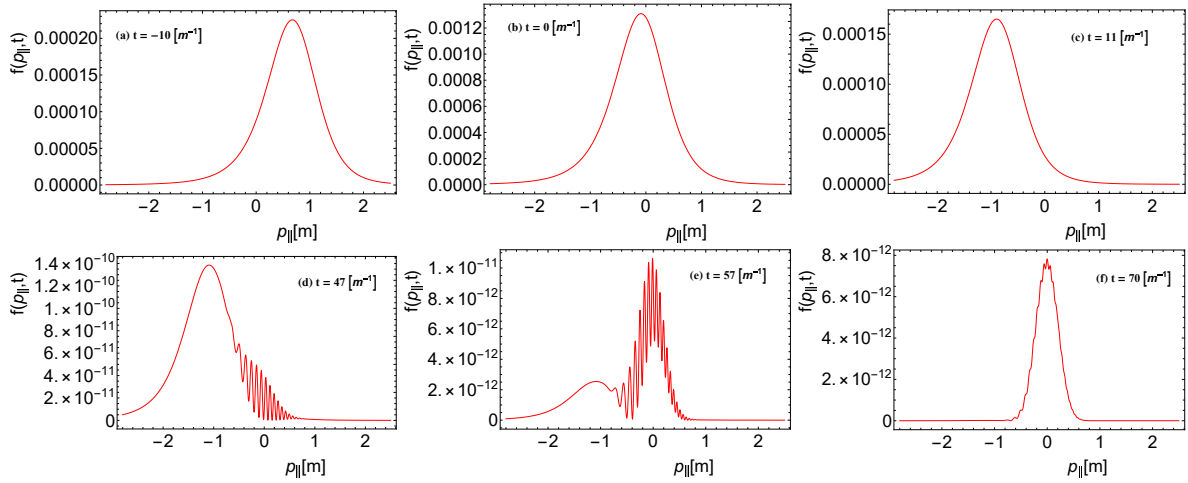


Figure 7: Time evolution of quasi-particle distribution function in the longitudinal momentum space  $f(p_{\parallel}, t)$ . The transverse momentum is considered to be zero, and all the units are taken in the electron mass unit. The field parameters are  $E_0 = 0.1E_c$  and  $\tau = 10[m^{-1}]$ .

profiles are observable. One of these profiles forms at the origin, potentially with the onset of oscillations. (ii) Short Pulse Behavior ( $\tau < 8$ ): In contrast, shorter pulses lead to a unique outcome. Initially, a smooth unimodal structure experiences a splitting near the REPP region. This leads to the formation of a multi-modal Gaussian structure, which eventually converges into a single-peaked Gaussian profile as time progresses towards the asymptotic state.

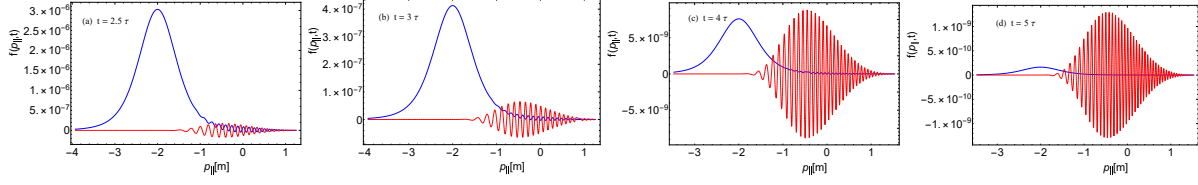


Figure 8: The first and second-order terms defined in (95) as a function of the longitudinal momentum for different times. Red curve :  $(1 - y)C_1$  and Blue curve:  $(1 - y)^2 C_2$ . The field parameters are  $E_0 = 0.1E_c$  and  $\tau = 10[m^{-1}]$ .

### 1. Approximate expression for longitudinal momentum distribution function

We aim to derive an expression for the longitudinal momentum distribution function  $f(p_{\parallel}, t)$  written as a series of  $(1 - y)$  up to second order, utilizing the approximate expression of the particle distribution function (91). We set  $p_{\perp} = 0$  throughout in this subsection.

$$f(p_{\parallel}, y) = |N^+(p_{\parallel})|^2 \left( C_0(p_{\parallel}, y) + (1 - y)C_1(p_{\parallel}, y) + (1 - y)^2 C_2(p_{\parallel}, y) \right) \quad (95)$$

Following eqs.(92), (93), and (94), it is evident that for  $t \gg 2\tau$ , the coefficients of  $(1 - y)$  and  $(1 - y)^2$  can be further approximated by retaining only the dominant contributions and disregarding the others, as follows:

$$C_0(p_{\parallel}, y) = 4y^2 \omega_1 (P_1 + \omega_1) |\Gamma_1|^2 \quad (96)$$

$$C_1(p_{\parallel}, y) \approx -\frac{4y|\Gamma_1 \bar{\Gamma}_2| E_0 \tau}{\sqrt{1 + (p_{\parallel} + E_0 \tau)^2}} \cos(\Upsilon) \quad (97)$$

$$\begin{aligned} C_2(p_{\parallel}, y) \approx & -\frac{4E_0^2 \tau^2 (p_{\parallel} + E_0 \tau - \sqrt{1 + (p_{\parallel} + E_0 \tau)^2})}{(1 + (p_{\parallel} + E_0 \tau)^2)} |\Gamma_1|^2 + 4\Gamma_1 \bar{\Gamma}_2 \cos \Upsilon \left( -1 - 3p_{\parallel}^2 + 3E_0^2 \tau^2 \right. \\ & + \frac{\sqrt{1 + (p_{\parallel} - E_0 \tau)^2} (1 + 3(p_{\parallel} + E_0 \tau)^2)}{\sqrt{1 + (p_{\parallel} + E_0 \tau)^2}} - \frac{4E_0^3 \tau^3 (4 + 3\tau^2 (1 + (p_{\parallel} + E_0 \tau)^2))}{(1 + (p_{\parallel} + E_0 \tau)^2)^{3/2} (4 + \tau^2 (1 + (p_{\parallel} + E_0 \tau)^2))} \\ & + \frac{3E_0 \tau}{\sqrt{1 + (p_{\parallel} + E_0 \tau)^2}} (-1 + (p_{\parallel} + E_0 \tau)^2 + \sqrt{1 + (p_{\parallel} - E_0 \tau)^2} \sqrt{1 + (p_{\parallel} + E_0 \tau)^2}) \\ & + E_0 \tau \frac{2\tau^2 \sqrt{1 + (p_{\parallel} + E_0 \tau)^2}}{4 + \tau^2 (1 + (p_{\parallel} + E_0 \tau)^2)} + \left( 3\sqrt{1 + (p_{\parallel} - E_0 \tau)^2} - 3\sqrt{1 + (p_{\parallel} + E_0 \tau)^2} \right. \\ & \left. - \frac{4E_0^2 \tau^2 (4 + 3\tau^2 (1 + (p_{\parallel} + E_0 \tau)^2))}{(1 + (p_{\parallel} + E_0 \tau)^2)^{3/2} (4 + \tau^2 (1 + (p_{\parallel} + E_0 \tau)^2))} \right) p_{\parallel} \end{aligned} \quad (98)$$

In Fig. 8, we depict the quantity  $(1 - y)^2 C_2$  as function of longitudinal momentum for different times ( $t > 2\tau$ ) and compare it with the first-order term  $(1 - y)C_1$ . Fig. 8 (a) shows that in earlier times, the second-order term dominates over the first-order term. The term  $(1 - y)^2 C_2$  displays an almost unimodal peak profile around  $p_{\parallel} \approx -2[m]$ , primarily due to  $|\Gamma_1|^2$  (see Eq.(98)), which depends on  $(E_0, \tau)$ , with its peak at  $p_{\parallel} \approx -E_0\tau$ . The oscillations observed in the range  $-1 < p_{\parallel} < 1$  can be explained by the presence of the second term in Eq. (98). This term contains a cosine function,  $\cos \Upsilon$ , which introduces oscillatory behavior. Additionally, it depends on both  $p_{\parallel}$  and  $t$ , contributing to the modulation of these oscillations within the specified range of  $p_{\parallel}$  as seen in Fig.8. As time progresses, we observe that the influence of the quantity  $(1 - y)C_1$  gradually increases compared to earlier times. This quantity exhibits oscillations within the Gaussian envelope, with the oscillations decaying as we move away from  $p_{\parallel} \approx 0$ . To understand the oscillations and how they depend on momentum and time, we approximate the cosine function as:

$$\begin{aligned}
\Upsilon = & \pi - \arctan(\tau) - \tau \ln(4) - 2\tau \ln(\tau) + \tau \ln(1 - y) \\
& + \frac{1}{2} \tau \left[ (1 + 2E_0\tau - \sqrt{1 + 4E_0^2\tau^2}) \ln[\tau(1 + 2E_0\tau - \sqrt{1 + 4E_0^2\tau^2})] \right. \\
& + (1 - 2E_0\tau + \sqrt{1 + 4E_0^2\tau^2}) \ln[\tau(1 - 2E_0\tau + \sqrt{1 + 4E_0^2\tau^2})] \\
& - (-1 + 2E_0\tau + \sqrt{1 + 4E_0^2\tau^2}) \ln[\tau(-1 + 2E_0\tau + \sqrt{1 + 4E_0^2\tau^2})] \\
& \left. + (1 + 2E_0\tau + \sqrt{1 + 4E_0^2\tau^2}) \ln[\tau(1 + 2E_0\tau + \sqrt{1 + 4E_0^2\tau^2})] \right] \\
& + \frac{E_0\tau^2}{\sqrt{1 + 4E_0^2\tau^2}} \ln \left[ \frac{-1 + \sqrt{1 + 4E_0^2\tau^2}}{1 + \sqrt{1 + 4E_0^2\tau^2}} \right] (p_{\parallel} + E_0\tau) \\
& + \frac{\tau}{4} \left[ 2 - \frac{2}{1 + \tau^2} - \frac{2}{1 + 4E_0^2\tau^2} - 4 \ln[2\tau] + \left( 1 - \frac{1}{(1 + 4E_0^2\tau^2)^{3/2}} \right) \ln[\tau(1 + 2E_0\tau - \sqrt{1 + 4E_0^2\tau^2})] \right. \\
& + \left( 1 + \frac{1}{(1 + 4E_0^2\tau^2)^{3/2}} \right) \ln[\tau(1 - 2E_0\tau + \sqrt{1 + 4E_0^2\tau^2})] + \ln[\tau(1 + 2E_0\tau + \sqrt{1 + 4E_0^2\tau^2})] \\
& + \frac{1}{(1 + 4E_0^2\tau^2)^{3/2}} \left( (-1 + \sqrt{1 + 4E_0^2\tau^2} + 4E_0^2\tau^2 \sqrt{1 + 4E_0^2\tau^2}) \ln[\tau(-1 + 2E_0\tau + \sqrt{1 + 4E_0^2\tau^2})] \right. \\
& \left. \left. + \ln[\tau(1 + 2E_0\tau + \sqrt{1 + 4E_0^2\tau^2})] \right) + 2 \ln(1 - y) \right] (p_{\parallel} + E_0\tau)^2 \tag{99}
\end{aligned}$$

up to quadratic term and neglecting other higher order.

From Eq. (99), we can see that the frequency of the oscillation depends on  $p_{\parallel}$ ,  $(1 - y)$  factor, and the field parameters  $(E_0, \tau)$ . Near  $p_{\parallel} = -E_0\tau$ , the cosine oscillation becomes flat, and its behavior near this point changes with time. However, it exhibits regular oscillation at points other than this (see Fig. 9).

We can see in Eq. (97) that there is a multiplication factor or amplitude of the  $\cos(\Upsilon)$  function that



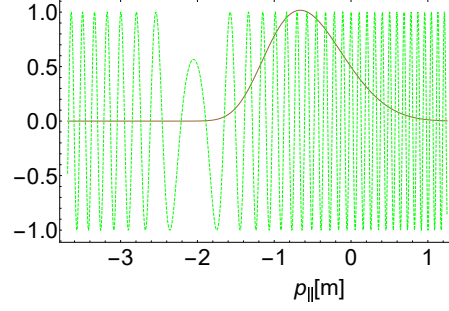


Figure 9: The individual components of  $C_1(p_{\parallel}, y)$  as defined in (97), as a function of longitudinal momentum, depicted for  $y \simeq 1$ ,  $E_0 = 0.2E_c$ , and  $\tau = 10[m]$ . The green dashed curve represents  $\cos(\Upsilon)$ , and the brown curve represents the amplitude function ( $A_{C1}$ ).

is also depends on momentum and time. This factor also influences the oscillatory behavior of the  $\cos(\Upsilon)$  function. To know its behavior, we compare these two functions by plotting for  $y \simeq 1$ , as shown in Fig. 9.

The amplitude of  $\cos(\Upsilon)$  function is given by:

$$\begin{aligned}
A_{C1}(p_{\parallel}) &= \frac{4|\Gamma_1\overline{\Gamma_2}|E_0\tau}{\sqrt{1+(p_{\parallel}+E_0\tau)^2}} \\
&\approx \frac{2E_0\tau e^{\frac{\pi}{2}(2E_0\tau-\sqrt{1+(p_{\parallel}-E_0\tau)^2}-\sqrt{1+(p_{\parallel}+E_0\tau)^2})}}{(1+(p_{\parallel}+E_0\tau)^2)\sqrt{1+\tau^2(1+(p_{\parallel}+E_0\tau)^2)}} \left( (1+(p_{\parallel}-E_0\tau)^2) \right. \\
&\quad \left. + \sqrt{1+(p_{\parallel}-E_0\tau)^2}(-p_{\parallel}+E_0\tau) \right) \quad (100)
\end{aligned}$$

$$\left. \frac{\partial A_{C1}}{\partial p_{\parallel}} \right|_{E_0=0.2, \tau=10} = 0 \quad (101)$$

This leads us to find that the maxima in this case occur at approximately  $p_{\parallel} \approx -0.6$ . Additionally, this function can be seen as nearly Gaussian, exhibiting almost symmetric characteristics. Fig. 9 confirms explicitly that the first-order term can be understood as a combination of a Gaussian envelope and an oscillatory component  $\cos \Upsilon$ . The behavior of this combined function exhibits an oscillation pattern in which the amplitude decreases as we move away from the peak position of the Gaussian envelope. The Gaussian envelope ensures a smooth decrease in the function, while the oscillatory component introduces periodic fluctuations in the amplitude. The frequency and amplitude of these oscillations depend on the parameters  $p_{\parallel}$ ,  $t$ , and  $(E_0, \tau)$ . At  $t = 4\tau$ , the magnitude of the first-order component dominates over the second-order, and its oscillation becomes faster, as seen in Figure 8(c). The second-order term diminishes at  $t = 5\tau$  (see Figure 8(d)). It's worth noting that both orders have a  $(1-y)$  factor, which contributes to the distribution function. However,

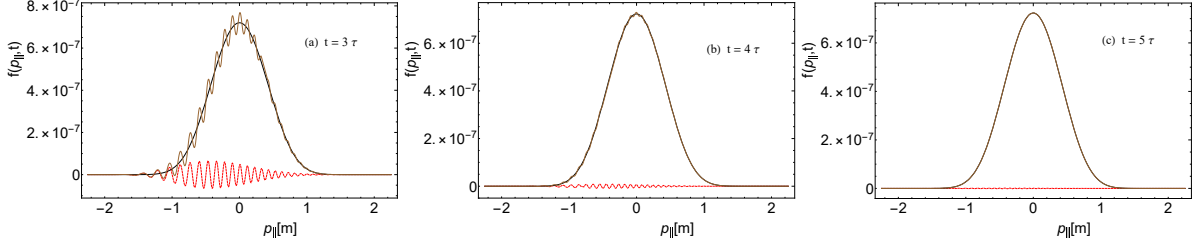


Figure 10: The zeroth and first-order terms defined in (95) as a function of the longitudinal momentum for different times. Black curve:  $C_0$  and Red curve :  $(1 - y)C_1$ , Brown curve:  $(C_0 + (1 - y)C_1)$ . The field parameters are  $E_0 = 0.2E_c$  and  $\tau = 10[m^{-1}]$ .

this contribution gradually decreases as time progresses, becoming less important for the late-time limit. In Figure 10, the comparison of  $C_1$ ,  $C_0$ , and  $(C_0 + (1 - y)C_1)$  is demonstrated to understand which order is responsible for the features of the longitudinal momentum distribution function in late times. At  $t = 3\tau$ ,  $C_0$  shows a smooth single peak located at  $p_{\parallel} = 0$ , while  $(1 - y)C_1$  exhibits oscillatory behavior within the small range  $-1 < p_{\parallel} < 1$ . The combined behavior resembles a smooth Gaussian structure with onset oscillation, contributing to the distribution function. This behavior is confirmed by a figure 10. As time progresses, the oscillation amplitude decreases due to the presence of the  $(1 - y)$  factor in the first-order component, reducing its impact. Additionally, the onset oscillation nearly disappears in the combined behavior. Consequently,  $C_0$  dominates and explains the distribution function's behavior at asymptotic time.

On careful examination of the individual components of the distribution function (95), we observe that during electron-positron formation at  $t > 2\tau$ , the second-order term  $((1 - y)^2C_2)$  is responsible for the primary peak located at  $p_{\parallel} \approx -2[m]$  (see Fig.5). As time progresses, this primary peak diminishes, and a secondary peak at  $p_{\parallel} = 0$  starts to build up due to the first-order term  $((1 - y)C_1)$  and zeroth-order term  $C_0$ , which are responsible for the onset oscillation on that peak. As time progresses towards infinity,  $C_1$  leads to suppression. Consequently, we observe only a secondary peak due to the dominance of the  $C_0$  zeroth-order term( see Fig.5). Since the component  $(1 - y)C_1$  represents an oscillatory finite function whose magnitude depends on  $t$ , the magnitude of this function plays a crucial role in determining the dynamics of  $f(p_{\parallel}, t)$  in  $p_{\parallel}$ -space at finite times. We further derive an asymptotic expression for the distribution function in the limit  $t \rightarrow \infty$  ( $y \approx 1$ ). The second and first-order terms become zero, and only zeroth order term( $C_0$ ) survive.

By lengthy calculations, we found an analytical expression for the distribution function for asymp-

otic times as follows:

$$\begin{aligned} f(p_{\parallel}, y \rightarrow 1) &= |N^+(p_{\parallel})|^2 C_0(p_{\parallel}) \\ &= 4\omega_1 |N^+(p_{\parallel})|^2 (\omega_1 + P_1) |\Gamma_1|^2 \end{aligned} \quad (102)$$

Using the eqs. (57) and (79), we obtain

$$f(p_{\parallel}, y \rightarrow 1) = \frac{2 \sinh(\pi\tau(2E_0\tau + \omega_0 - \omega_1)/2) \sinh(\pi\tau(2E_0\tau - \omega_0 + \omega_1)/2)}{\sinh(\pi\tau\omega_0) \sinh(\pi\tau\omega_1)} \quad (103)$$

The particle distribution function coincides with the results reported in earlier studies on the asymptotic particle distribution function [63, 80]. This distribution function is symmetric about the momentum in the direction of the applied electric field. By approximating the  $\omega_1$  and  $\omega_0$  as series expansion around  $p_{\parallel} = 0$  up to quadratic order and neglecting higher order and further simplifying, we get

$$f(p_{\parallel}) \approx 2e^{2\pi\tau(E_0\tau - \sqrt{1+E_0^2\tau^2})} \exp\left\{-\pi \frac{p_{\parallel}^2 \tau}{(1 + E_0^2\tau^2)^{3/2}}\right\} \quad (104)$$

Next, we analyse the qualitative picture of LMS at finite time for Keldysh parameter,  $\gamma = 1$  as we discuss in previous subsection this using the two different configurations of parameters  $E_0$  and  $\tau$  shows its impact on finite-time behavior of LMS. We observe that LMS shows multi-peaks for  $\tau = 5[m^{-1}]$  and bi-modal Gaussian-like profile with one have onset oscillations for  $\tau = 8[m^{-1}]$  as seen in Fig.7. We can understand this trends using the  $\Upsilon$  that present in the first and second-order terms of particle distribution function relation (95). We can approximate the argument,  $\Upsilon$  as series expansion around  $p_{\parallel} = 0$  as follows:

$$\begin{aligned} \Upsilon &\approx \pi - \tan^{-1}\left(\frac{\tau}{\gamma} \sqrt{1 + \gamma^2}\right) + \frac{\tau}{\gamma} \ln\left(\frac{\sqrt{1 + \gamma^2} + 1}{\sqrt{1 + \gamma^2} - 1}\right) + \sqrt{1 + \gamma^2} \ln\left(\frac{\gamma^2(1 - y)}{1 + \gamma^2}\right) \\ &+ p_{\parallel} \frac{\tau}{\sqrt{1 + \gamma^2}(\tau^2 + \gamma^2(1 + \tau^2))} \left(\ln\left(\frac{(1 - y)}{1 + \gamma^2}\right)(\gamma^2(1 + \tau^2) + \tau^2) - \gamma^2\right) \\ &+ p_{\parallel}^2 \sqrt{1 + \gamma^2} \gamma \tau \left(\frac{\gamma^2 \tau^2 (2 + \gamma^2 - \gamma^4) - \gamma^6}{(\gamma^2(1 + \tau^2) + \tau^2)^2} - 2 + \frac{\gamma^2}{2(1 + \gamma^2)} \ln\left(\frac{\gamma^2(1 - y)}{1 + \gamma^2}\right)\right) \end{aligned} \quad (105)$$

From the above equation, Eq. (105) shows that the argument of the cosine function depends on the values of the pulse duration,  $\tau$ , and the  $\gamma$  parameter. For a given Keldysh parameter, the momentum frequency of oscillation purely depends on  $\tau$ . As we decrease  $\tau$ , the frequency of oscillation also decreases, resulting in oscillations in the momentum spectrum as seen in Fig. 6. For small values of  $\tau$ , the number of oscillations decreases according to Eq. (105), leading to a multi-peak structure seen in the spectrum.

## 2. LMS in the multi-photon regime

In this section, we explored the LMS of the created particle in the multiphoton regime. We choose the parameters of the laser pulse in such a way that the Keldysh parameter,  $\gamma \gg 1$ . Fig. 11 shows LMS for short pulse-duration  $\tau = 4[m^{-1}]$  and  $E_0 = 0.1E_c$ . The Keldysh parameter, in this case, is close to 2.5, i.e.,  $\gamma \gg 1$  corresponds to  $n^{\text{th}}$  order perturbation theory, with  $n$  being the minimum number of photons to be absorbed in order to overcome the threshold energy for pair creation  $n\omega > 2m$ . In the early time of the creation of pairs,  $t = -4[m^{-1}]$ , spectrum has a unimodal Gaussian-like profile peak at  $p_{\parallel} \simeq -0.4$ , and as time proceeds, we see shifting of peak  $p_{\parallel} \simeq -eE_0\tau$  to  $p_{\parallel} \simeq eE_0\tau$  due to the action of Lorentz force and its peak value shows the maximum value for  $t = 0$ , i.e.,  $f(p_{\parallel}) = 1.4 \times 10^{-3}$  (see figure 11 (a-c)). However, that smooth unimodal spectrum now shows slight modulation Fig. 11(d) when  $t = 9[m^{-1}]$  (which is greater than the effective pulse duration length ( $2\tau$ )). At finite time,  $t = 12[m^{-1}]$  spectrum has a quad-modal profile, as seen in figure 11(e). The central peak, which is located at  $p_{\parallel} = 0$ , is much more prominent than the two unequal peaks at  $p_{\parallel} \simeq \pm 0.4[m]$  and another very small peak at  $p_{\parallel} \simeq 0.7[m]$ . Fig. 11(f-g) shows the merging of those multimodal peaks as a result of the fading of different peaks that occur and the single smooth Gaussian peaks observed at  $t > 5\tau$  as shown in figure 11 (h-i).

An interesting qualitative contrast becomes evident when comparing the previous scenario with  $\gamma = 0.5$  to the current situation. The presented figure illustrates this distinct behavior. Notably, a multi-modal pattern emerges at a specific moment, characterized by the presence of more than two peaks, occurring approximately at  $3\tau$ .

As discussed in the previous section, the characteristic features of the LMS can be mathematically explained using a simple approximate function, as shown in Eq. (95). Similar analysis can help us understand the behavior of the multiple peaks observed in the LMS at finite time.

In multi-photon case,  $E_0\tau < 1$ , the first-order term becomes

$$C_1(p_{\parallel}, y) \approx A_{C1}(p_{\parallel}) \cos(Y) \quad (106)$$

where,

$$\begin{aligned} A_{C1}(p_{\parallel}) = & \frac{1}{2} e^{\frac{\pi}{2}(E_0\tau(2-E_0\tau)-2)} e^{p_{\parallel}^2(1-E_0^2\tau^2)} (4 + 2E_0\tau(2 - E_0\tau - 2E_0^2\tau^2)) + p_{\parallel}^2(-2 + E_0\tau(12 + 57E_0\tau)) \\ & + 2p_{\parallel}(-2 - 10E_0\tau - 6E_0^2\tau^2 + 15E_0^3\tau^3) \end{aligned} \quad (107)$$

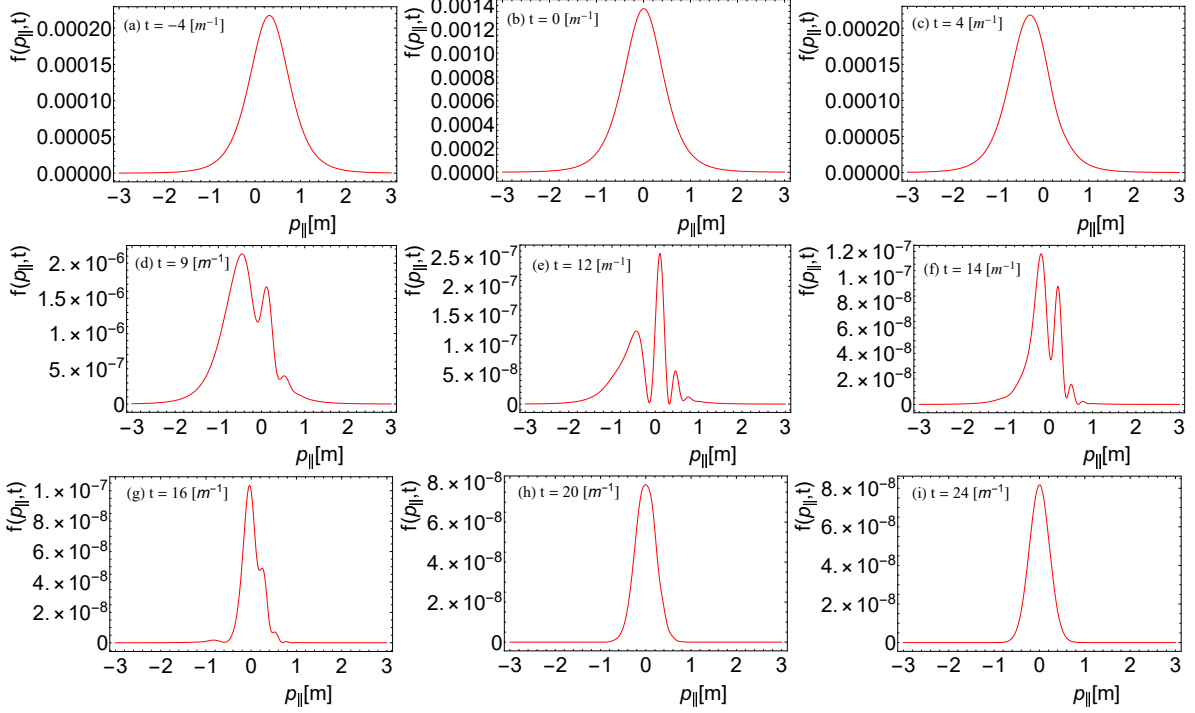


Figure 11: Time evolution of quasi-particle distribution function in the longitudinal momentum space  $f(p_{\parallel}, t)$  at different times. The transverse momentum is considered to be zero, and all the units are taken in the electron mass unit. The field parameters are  $E_0 = 0.1E_c$  and  $\tau = 4[m^{-1}]$ .

$$\begin{aligned}
\Upsilon \approx & E_0\tau^2 \ln\left(\frac{E_0\tau + \sqrt{1 + E_0^2\tau^2}}{-E_0\tau + \sqrt{1 + E_0^2\tau^2}}\right) + \tau\sqrt{1 + E_0^2\tau^2} \ln\left(\frac{(1-y)}{1 + E_0^2\tau^2}\right) \\
& + p_{\parallel}\tau \frac{E_0\tau}{\sqrt{1 + E_0^2\tau^2}} \ln\left(\frac{E_0^2\tau^2(1-y)}{1 + E_0^2\tau^2}\right) + \frac{p_{\parallel}^2\tau}{2(1 + E_0^2\tau^2)^{3/2}} \left(-2E_0^2\tau^2 + \ln\left(\frac{(1-y)}{1 + E_0^2\tau^2}\right)\right) \quad (108)
\end{aligned}$$

In the Fig. 12 for the given field parameters, we observe a decrease in the oscillation frequency for the  $\cos(\Upsilon)$  function compared to the previous case  $\gamma = 0.5$  (see Fig. 12). As the oscillation frequency decreases for smaller values of  $\tau$ , it also reflects in the LMS of created particles as a lack of oscillatory features. Near  $p_{\parallel} = -E_0\tau$ , the cosine function behaves irregularly, flattening out, and oscillates regularly away from this point. The  $A_{C1}$  function (107) plays a crucial role here, resembling a Gaussian single peak structure whose peak location occurs at  $p_{\parallel} = -0.1[m]$  represented by the brown curve in Fig. 12. The width of the Gaussian envelope and its peak location affect the behavior of the  $\cos(\Upsilon)$  within the envelope. Consequently, the presence or absence of oscillations in the envelope depends on the field parameters, which influence the amplitude function  $A_{C1}$  peak and the  $\cos(\Upsilon)$  function's behavior.

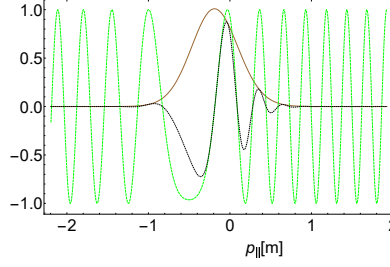


Figure 12: The first order term,  $C_1$  and its individual components as defined in Eq.(106), as a function of longitudinal momentum, depicted for  $y \approx 1$ ,  $E_0 = 0.2E_c$ , and  $\tau = 10[m^{-1}]$ . The green dashed curve represents  $\cos(\Upsilon)$ , the brown curve represents the amplitude function ( $A_{C1}$ ) and black dotted curve represents  $C_1$ .

We can understand that the appearance of multiple peaks in the spectrum is the combined effect of the oscillation of the cosine function and the amplitude function, as seen in Fig. 12 by the black curve, which shows that fewer irregular oscillations occur due to the first-order term  $C_1$ , and becomes suppressed in the long-time limit. As a result, the multi-modal pattern gradually dissipates, eventually leading to a singular smooth peak above  $t > 5\tau$ . Intriguingly, a similar evolution is observable in the case of  $\gamma = 0.5$ , signifying a shared progression in both scenarios despite representing a non-multiphoton process.

### C. Vacuum Polarisation and depolarisation function

For a better understanding of the phenomenon of particle creation under the strong electric field, we will also trace the evolution of the vacuum polarization function,  $u(\mathbf{p}, t)$  its counter term  $v(\mathbf{p}, t)$ . Figure 13 shows the time evolution of  $u(p_{\parallel}, t)$  and  $v(p_{\parallel}, t)$  for different values of  $p_{\parallel}$  at zero transverse momentum. Due to pair annihilation being stronger than pair creation in the early times, depolarisation function  $v(p_{\parallel}, t)$  dominates over  $u(p_{\parallel}, t)$ [13(a) – (c)]. It appears that in the polarization function, there is a sinusoidal-type structure. On the other hand, the depolarization function  $v(p_{\parallel}, t)$  shows an unimodal Gaussian peak structure in its temporal evolution. Both  $u(p_{\parallel}, t)$  and  $v(p_{\parallel}, t)$  show oscillations with varying amplitudes during the initial transient stage. These oscillations are particularly pronounced when  $p_{\parallel} = 0[m]$ , as evident from figure 13(a) and 13(c). As time progresses, irregular oscillations are observed in the transient stage. However, the oscillations become regular and stable as the system enters the REPP stage. Both functions,  $u(p_{\parallel}, t)$  and  $v(p_{\parallel}, t)$ , now exhibit regular oscillations centered around the zero value. Moreover, as the momentum value  $p_{\parallel}$  increases, the amplitudes of these oscillations diminish, as shown in

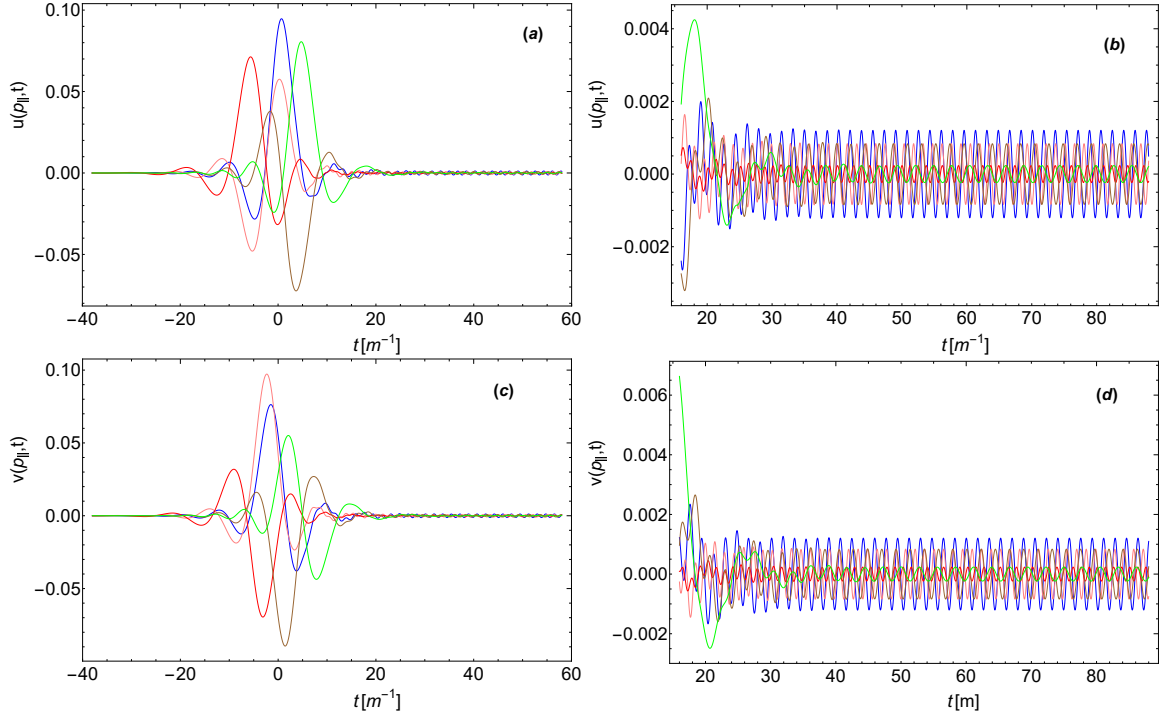


Figure 13: Evolution of  $u(t, p_{\parallel})$  and  $v(t, p_{\parallel})$  for  $p_{\parallel} = 0$  (blue),  $0.5$  (pink),  $-0.5$  (brown),  $1$  (red),  $-1$  (green) with  $p_{\perp} = 0$ ,  $E_0 = 0.2E_c$  and  $\tau = 10[m^{-1}]$ . All the measurements are taken in electron mass units.

figure 13(b) and 13(d). During the REPP stage, one interesting finding is that  $u(p_{\parallel}, t)$  and  $v(p_{\parallel}, t)$  demonstrate balancing behavior characterized by similar oscillatory patterns. This balance results from the formation of real independent pairs of electron-positrons.

### 1. Momentum Spectra of $u(p_{\parallel}, t)$ and $v(p_{\parallel}, t)$

The longitudinal momentum significantly impacts the vacuum polarization function's qualitative traits. To understand its dependence on  $p_{\parallel}$ , we comprehensively analyze the momentum spectra of both  $u(p_{\parallel}, t)$  and its associated counter term  $v(p_{\parallel}, t)$ . Figure 14 displays the LMS of  $u(p_{\parallel}, t)$  and  $v(p_{\parallel}, t)$ . In the initial stages of particle formation, specifically at  $t < 0$ ,  $u(p_{\parallel}, t)$  and  $v(p_{\parallel}, t)$  display asymmetric Gaussian peaks with roughly similar profiles. During this period,  $v(p_{\parallel}, t)$  dominates over  $u(p_{\parallel}, t)$ . Upon closer examination, it becomes evident that the peaks occur at different positions around  $p_{\parallel} \approx 1[m]$ , as illustrated in Figure 14(a). At  $t = 0[m^{-1}]$ , the initial Gaussian-shaped structure of  $u(p_{\parallel}, t)$  deformed, becoming a bi-modal asymmetric Gaussian-like structure.  $u(p_{\parallel})$  displays peaks at specific non-zero values of  $p_{\parallel} \approx -0.35[m]$  and a dip (or valley)

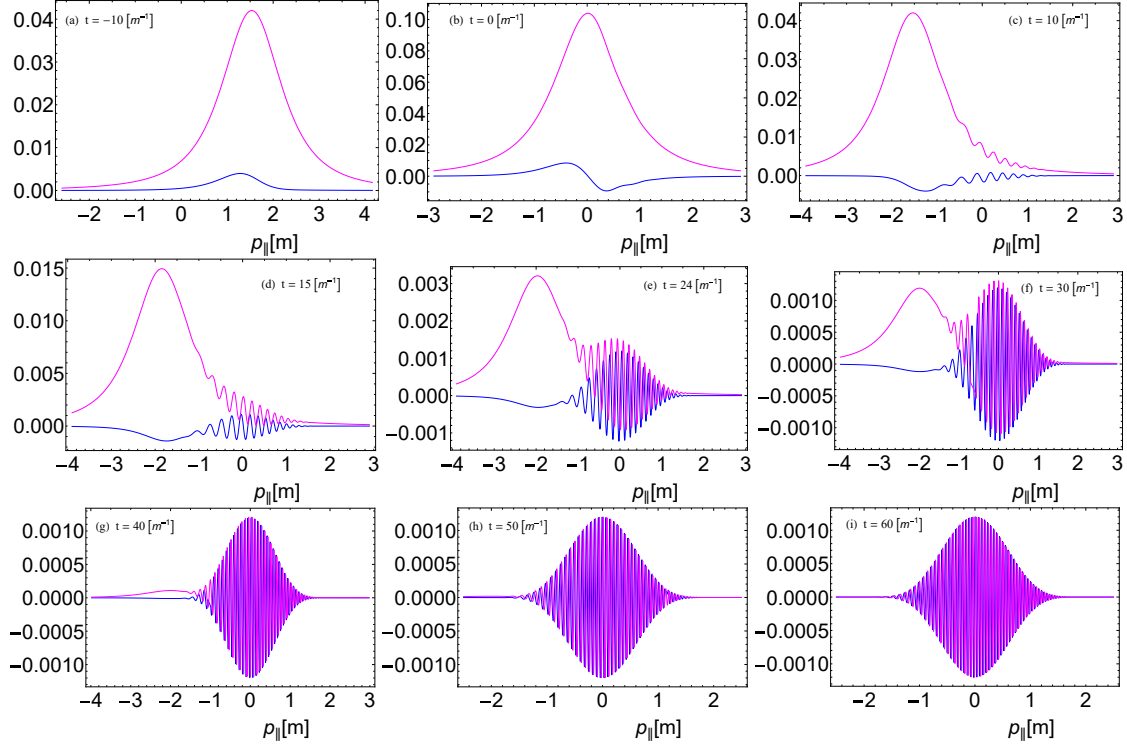


Figure 14: Created particle LMS at finite time Blue curve: polarisation function(  $u(p_{\parallel}, t)$  ) and Magenta curve: de-polarisation function(  $v(p_{\parallel}, t)$  ). The transverse momentum is considered zero, and all the units are taken in the electron mass unit. The field parameters are  $E_0 = 0.2E_c$  and  $\tau = 10[m^{-1}]$ .

at  $p_{\parallel} \simeq +0.35[m]$ . In contrast, the  $v(p_{\parallel}, t)$  spectrum retains its Gaussian-like unimodal profile, with the peak at  $p_{\parallel} = 0[m]$ . The behavior of  $u(p_{\parallel}, t)$  undergoes significant changes, becoming asymmetric, while  $v(p_{\parallel}, t)$  remains unchanged in its overall shape during this stage. Due to the force factor “ $eE(t)$ ” and corresponding longitudinal quasi-momentum  $P(t) = (p_{\parallel} - eA(t))$ , the spectrum moved to the left side of the origin, and its peak now located at  $p_{\parallel} \approx -2[m]$  for  $v(p_{\parallel}, t)$  whereas small dip in LMS of  $u(p_{\parallel}, t)$  with some disruption in the tail ( $-1 < p_{\parallel} < 1$ ) as shown in the figure 14(c-d) near to the transient stage. The behavior of  $v(p_{\parallel}, t)$  and  $u(p_{\parallel}, t)$  at this stage explicitly counter each other, as they exhibit distinct shifts and variations due to the applied electric field and longitudinal quasi-momentum. At  $t = 24[m^{-1}]$ , we observe two distinct structures in the polarization and depolarization functions as time progresses. The first structure occurs at  $p_{\parallel} = -2[m]$ , as a consequence of earlier vacuum excitation responsible for pair formation. The second structure is located in the range  $-1 < p_{\parallel} < 1$ , exhibiting varying amplitude oscillations, with the maximum occurring at zero longitudinal momentum throughout the process. At this stage,  $u(p_{\parallel})$  and  $v(p_{\parallel})$  compete with each other, as shown in Figure 14(d) and 14(e). As we approach the beginning of the REPP stage, both functions,  $u(p_{\parallel}, t)$  and  $v(p_{\parallel}, t)$ , indeed exhibit a single oscillating structure



resembling a sine or cosine function with varying amplitude. The maximum now appears near  $p_{\parallel} = 0$ , dominating in comparison to the secondary peak (and dip for  $u(p_{\parallel}, t)$ ) that was present on the left side of the origin at  $p_{\parallel} \approx -2[m]$ . As time progresses further, this left side structure slowly vanishes, as shown in Figure 14(e) and 14(f). Eventually, as  $A(t)$  reaches a constant value, a balance is achieved between the processes of particle creation and annihilation, as depicted in Figure 14(g). In the late REPP stage, where the particle distribution function  $f(p_{\parallel}, t)$  is constant, the polarization function  $u(p_{\parallel}, t)$  is balanced by its counterpart  $v(p_{\parallel}, t)$ . This results in very regular and rapid oscillations with varying amplitude within the Gaussian envelope, as explicitly shown in figure 14(h-i). During this stage, the system exhibits a stable oscillatory behavior, indicating a well-established equilibrium between particle creation and annihilation processes. The overall behavior observed in both  $u(p_{\parallel}, t)$  and  $v(p_{\parallel}, t)$  during this process provides valuable insights into the complex dynamics of particle-antiparticle pair creation and annihilation under the influence of the electric field.

## 2. Examining quantum interference effect in LMS of $f(p_{\parallel}, t)$ : Role of Vacuum Polarization and Depolarization Functions

During the formation of electron-positron pairs from the quantum vacuum, various processes can occur. Electrons are prominently produced and annihilated simultaneously, resulting in electron acceleration and deceleration throughout the formation of real  $e^-e^+$  independent pairs from the virtual  $e^-e^+$  pairs. In this situation, polarization functions  $u(\mathbf{p}, t)$  and its counter term  $v(\mathbf{p}, t)$  are responsible for the acceleration and deceleration of electrons, respectively. In that sense, when an electron is typically created in the direction of the external field with positive momentum and are subsequently decelerated and may then, as soon as  $p_{\parallel} < 0$ , be annihilated again; these processes can be understood in terms of  $u(\mathbf{p}, t)$  and  $v(\mathbf{p}, t)$  which represents the acceleration and deceleration of electrons. In quasi-momentum space, there are many possibilities that particles can find with specific momentum  $p_0$  with time  $t_0$ . Suppose particles at a lower momentum level with  $(p_0 - \delta p_0)$  in earlier time reach momentum value  $p_0$  by acceleration process showed by  $u(p_{\parallel}, t)$  and it is also possible that particles at higher momentum level with  $(p_0 + \delta p_0)$  followed by deceleration process  $(p_0 - \delta p_0)$  and finally come to momentum value  $p_0$  see figure 15.

In the LMS at a specific time  $t_0$ , two possible events can give rise to the quantum interference effect. This expectation is explicitly confirmed in the middle panel of figure 5, where oscillations are observed in a bell-shaped profile around  $t \approx 2\tau$ . These oscillations in the LMS are observed for

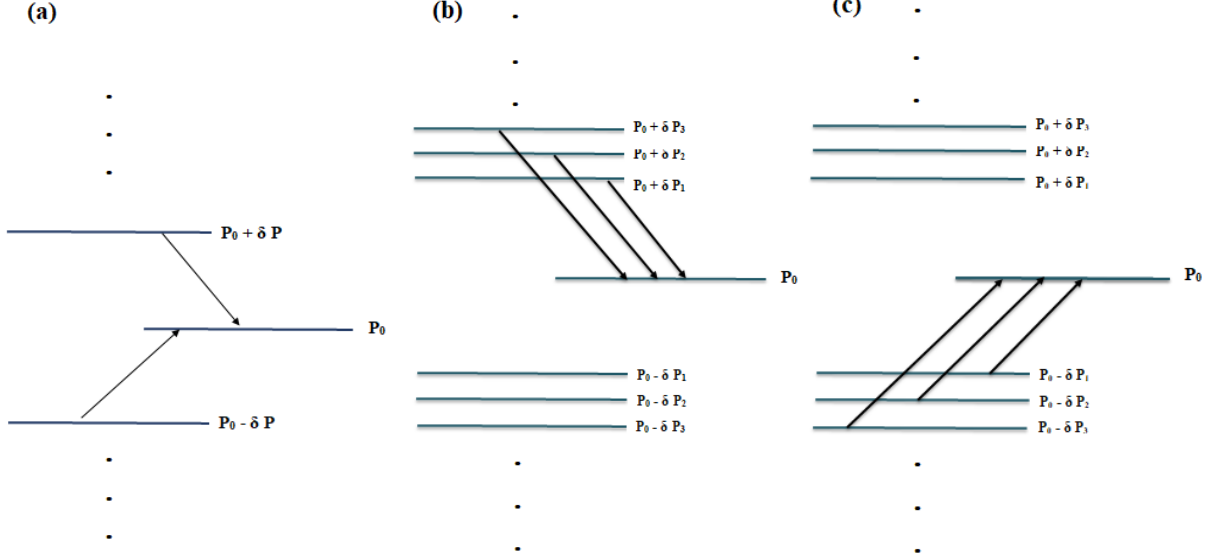


Figure 15: A schematic representation of particle occupies different momentum states in different scenarios

a very short duration, during which coherence is maintained in the LMS of  $u(p_{\parallel}, t)$  and  $v(p_{\parallel}, t)$ , as evident from Figure 14(e-f). However, these oscillations slowly fade away in the late REPP region around  $t = 4\tau$ . The disappearance of oscillations in the particle LMS can be understood in terms of the loss of coherence that was maintained in the LMS of  $u(p_{\parallel}, t)$  and  $v(p_{\parallel}, t)$ . After the loss of coherence, the LMS of  $u(p_{\parallel}, t)$  and  $v(p_{\parallel}, t)$  become identical at  $t = 6\tau$  (see Figure 14 (i)). The envelope of the Gaussian with a cosine or sine variation results in a smooth bell-shaped particle momentum distribution. This behavior suggests a well-established equilibrium in the system, with interference effects subsiding and a stable particle-antiparticle distribution being achieved.

#### D. Dependence on Transverse momentum

In this section, we extensively investigate the effect of transverse momentum on particle distribution function in dynamical stages of pair production by plotting the time evolution of the LMS for different fixed values of transverse momentum ( $p_{\perp}$ ), and the result is displayed in Fig.16. The spectra exhibit a smooth unimodal structure during the initial stages, as depicted in Fig.16(a). Notably, the peak's location shifts, as illustrated in Fig.16(b), accordingly with the  $(p_{\parallel} - eA(t)) = 0$  as explained in Sec.IV B. Within a narrow spectral region for  $-1 < p_{\parallel} < 1$ , some irregular oscillating structure is observed. Furthermore, these figures indicate that the peak value of the spectra decreases with the increase in the value of transverse momentum.

Fig. 16 (c), at  $t = 30[m^{-1}]$  spectra shows bimodal distribution. The central peak structure

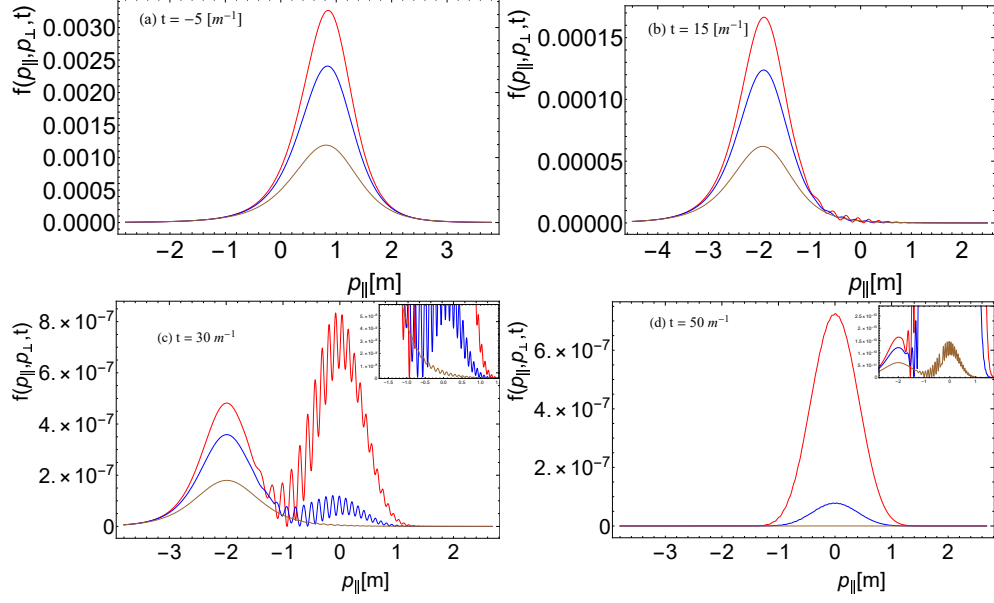


Figure 16: LMS of created particles for different values of the transverse momentum  $p_{\perp}$  ( $p_{\perp} = 0$ (red),  $p_{\perp} = 0.4$ (blue), and  $p_{\perp} = 0.8$  (brown).)

with onset oscillation located at  $p_{\parallel} = 0[m]$  dominates over another peak at  $p_{\parallel} = -2[m]$  for a small value of  $p_{\perp}$ . One interesting fact observed that the central peak magnitude diminished very rapidly compared to other peaks and that oscillating structure does not exist for high transverse momentum at this time. The existence of oscillation in the central peak depends on what time the particle reaches the on-shell configuration from the initial off-shell mass configuration, which critically depends on both transverse as well as longitudinal momentum values explained in Sec. IV A. Overall we know that from Sec.IV A on increasing the momentum value particle takes a

$p_{\perp}[m]$	$t_{cp}[m^{-1}]$	$t_{sep}[m^{-1}]$	$t_{dis.}[m^{-1}]$
0.00	22	30	50
0.25	24	32	53
0.50	31	38	63
0.75	39	47	71
1.00	53	60	83

Table III: Impact of Transverse Mode on Different Time Scale. The time scale  $t_{cp}$  appearance of a central peak,  $t_{sep}[m^{-1}]$  when two peaks become distinctly separated, and  $t_{dis.}$  disappearance of the oscillation in LMS.

longer time to reach in REPP stage. So, depending upon the value of  $(p_{\parallel}, p_{\perp})$  we can say that

different portions of spectra point to the different dynamical stages. The insets of Fig. 16 (c) shows only irregular oscillatory structure in the tail region of spectra for  $p_{\perp} = 0.8[m]$ , and the central peak structure is not observed. This absence is attributed to the fact that particles are in the QEPP stage for higher transverse values. At  $t = 50[m^{-1}]$ , for  $p_{\perp} = 0$ , that oscillation is nearly smooth, but for high transverse value,  $p_{\perp} = 0.8[m]$  magnitude of peak diminished see Fig.16 (d), however as shown in insert figure that onset oscillation still observed only magnitude get decreased. From this observation, we can say that the Central peak structure does not show the same behavior for a higher value of  $p_{\perp}$ , this is what exactly is implied by Fig. 16 (d). As we see that for higher transverse momentum, we still see that central peak with onset oscillation, which means it just reaches the REPP region. We also observe that for a higher value of  $p_{\perp}$  width of the spectra,  $\Delta p_{\parallel}$  gets decreased see insert Fig. 16 (d). From the occurrence of that oscillation structure or quantum interference patterns, as we previously identified some time scales discussed in subsection IV B, we now observe that the quantum signature depends on the transverse momentum, as indicated in Table 3. Lower  $p_{\perp}$  values exhibit oscillation patterns that become visible earlier than higher momenta.

### E. Transverse Momentum Spectrum

Following our exploration of how transverse momenta impact the longitudinal momentum distribution of produced particles, we now shift our attention toward examining the transverse momentum spectrum (TMS) of created particles. Fig.17 shows the time evolution of TMS of created particles for the longitudinal momentum value  $p_{\parallel} = 0$ . TMS shows a single peak structure at  $t = -5[m^{-1}]$ , ( see fig.17(a) ) where the electric field just reached 75% of its maximal strength. As the electric field attains maximum value at  $t = 0$  and its result  $f(p_{\perp}, t = 0)$  also shows maximum peak value as seen in Fig. 17 (b). After reaching to maximum value distribution function,  $f(p_{\perp}, t = 0)$  rapidly decreases as the electric field decreases. The spectra which have a single-peak structure become distorted at  $t \approx 5[m^{-1}]$  which is equivalent to half of the pulse width,  $\tau$ . As an example, at  $t = 7[m^{-1}]$  the initially smooth unimodal structure has changed. The peaks that were initially observed at  $p_{\perp} = 0$  are now absent, replaced by a noticeable dip, and new peaks have emerged at  $p_{\perp} = \pm 0.5[m]$  see Fig. 17 (c). The momentum distribution function shows the symmetric behaviour,  $f(p_{\perp}) = f(-p_{\perp})$ . Due to the dependence on transverse momentum through the transverse energy  $\epsilon_{\perp}(p_{\perp}) = \sqrt{m^2 + p_{\perp}^2}$ . The small peaks at  $p_{\perp} = \pm 0.49[m]$  tend to merge as time proceeds and give rise peak at  $p_{\perp} = 0$  with some new small peaks (see Fig.17(d)).

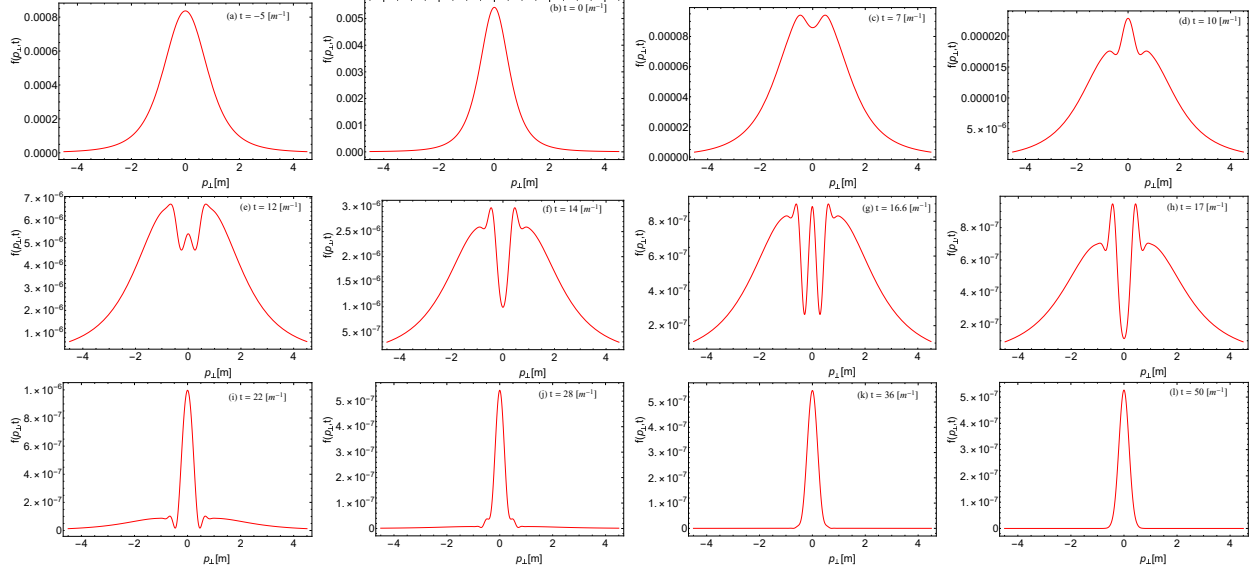


Figure 17: TMS of created particles in the presence of time-dependent Sauter pulse at different times. The longitudinal momentum is considered to be zero, and all the units are taken in the electron mass units. The field parameters are  $E_0 = 0.2E_c$  and  $\tau = 10[m^{-1}]$ .

Small side peaks grow as time progresses, and the central peak magnitude is lowered as seen in Fig.17 (e) at  $t = 12[m^{-1}]$ , spectra show maximum peak value at non-zero value  $p_{\perp} = \pm 0.65[m]$  and also observe one small peak at  $p_{\perp} = 0[m]$ . Once again, at  $t = 14[m^{-1}]$ , the spectrum exhibits a maximum peak at a non-zero value, i.e.,  $p_{\perp} = \pm 0.5[m]$  and other smaller side peaks at  $p_{\perp} \approx \pm 1[m]$ , as depicted in Fig.17 (f). At  $p_{\perp} = 0$ , a dip is evident, and as time progresses, multiple peaks become observable in the spectrum. For instance, at  $t = 16.6[m^{-1}]$ , as illustrated in Fig.17 (g). The spectrum undergoes continuous changes, manifesting two distinct structures. One scenario involves a maximum peak at  $p_{\perp} = 0[m]$ , indicating particles with no transverse momentum. The other scenario features the maximum peak of spectrum occurring at non-zero  $p_{\perp}$ -value, and in both situations, multiple peaks are observed in the spectrum see figure 17. The effect of created pairs tends to have a peak of momentum distribution function at non-zero transverse momentum, as discussed by Krajewska et al. [81]. It is demonstrated that the transverse momentum distribution of real pairs exhibits an off-axis maximum above the one-photon threshold frequency (or high frequency); otherwise, the maximum for the transverse distribution function occurs at  $p_{\perp} = 0$  in the presence of an oscillating time-dependent electric field.

Moreover, in our scenario, the presence of off-axis maxima in the spectrum is not observed during the REPP stage; instead, it is evident only before the REPP stage. The presence of this substructures in the spectrum at the QEEP and near to transient stage depends upon the specific

value of momenta. As the particle reaches the REPP stage, the spectrum shows a prominent peak at zero transverse momentum, accompanied by weakly pronounced peaks at  $p_{\perp} \approx \pm 0.67[m]$  and  $p_{\perp} \approx \pm 0.84[m]$  as seen in the figure 17(i). The width of the momentum spectra changes with time. The half-width of the  $p_{\perp}$ -distribution is determined by the field strength at that time, which is explicitly confirmed by figure 17. As the electric field decays to 98.6% of its maximum value, the width of the  $p_{\perp}$  distribution becomes of the order of 1, and the substructure in TMS disappears in the REPP stage ( see fig.17 (j)). At this stage, the TMS shows a smooth Gaussian-like distribution, with the maximum value  $f(p_{\perp}, t)$  occurring at  $p_{\perp} = 0$  as shown in figure 17(k). In the absence of an electric field, the spectrum exhibits a single peak Gaussian-like structure that remains unchanged, and also the distribution function  $f(p_{\perp})$  can be well understood by assuming that particle creation is exponentially suppressed with  $\exp(-\frac{m^2+p_{\perp}^2}{eE_0})$  see Fig. 17(l) transversal particle spectrum shows a Gaussian distribution. This contrast highlights the dynamic evolution of substructures in initial stages, contrasting with the smooth Gaussian-like structure observed in the REPP stage. Similar kinds of non-trivial features in the transverse momentum distribution are observed, depending on the details of the electric field parameters discussed by Bechler et al.'s work [82], in which the TMS of generated particles reveals a fascinating characteristic—off-axis maxima above the one-photon threshold frequency (or high frequency). The authors further discuss the significant changes in energy distribution between created particles' longitudinal and transverse motion. This raises questions about the feasibility of pair formation through tunneling theory, given the substantial distribution function values at non-zero transverse momentum but for low frequencies. In our specific case, we can see that the asymptotic distribution function is described as the Schwinger-like formula as we see later in sec.IV E 1. Also, the particle distribution function shows a maximum value where the transverse momentum becomes negligible. An intriguing aspect is that the tunneling time of particles is altered due to the increase in transverse momentum. This observation is substantiated by the fact that the occurrence of the transient stage is influenced by the momentum values  $(p_{\parallel}, p_{\perp})$ , as explained in section IV A.

Next, we investigate the impact of longitudinal momentum on TMS at finite time. We observe the interesting feature that different longitudinal values manifest distinct substructures in the spectrum at a fixed time as explicitly verified from Figs.18(a). The magnitude of the distribution function decreases for higher longitudinal momentum. Before particles reach the on-shell condition, the spectra of created particles at times  $t < 3\tau$  exhibit a dramatic change in structure, contingent on the value of  $p_{\parallel}$ . In this sense, we can say that the motion of the longitudinal and transverse directions are strongly coupled and its impact is easily seen in Figs.18(b). These concerns can be understood

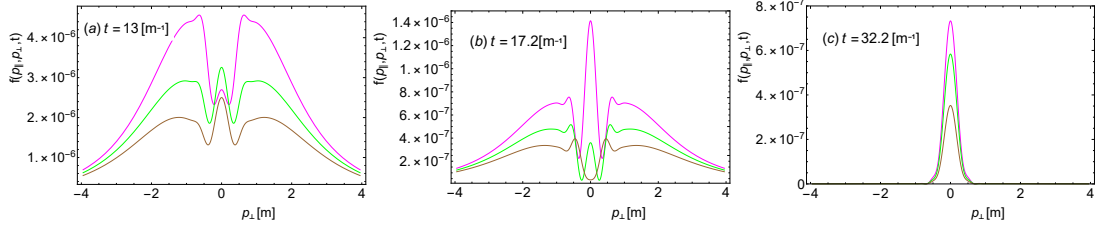


Figure 18: TMS of created particles for different values of the longitudinal momentum  $p_{\parallel}$  ( $p_{\parallel} = 0.1$ (magenta),  $p_{\parallel} = 0.3$ (green), and  $p_{\parallel} = 0.5$  (brown).)

through the quasi-energy  $\omega(p_{\parallel}, p_{\perp}, t)$  through which longitudinal and transverse motion of created particles are related. At the REPP stage, the substructure in the spectrum disappears and the peak height for higher longitudinal momentum value is consistently lower shown in Fig.18(c).

### 1. Approximate expression for transverse momentum distribution function

In this subsection, we discuss the mathematical origin of the substructures that appear in the TMS. Using the approximate analytical expression of the one-particle distribution function in momentum space, which is derived in Sec.III C, we determine the approximate expression for the transverse momentum distribution function and take the longitudinal momentum value to zero. In this condition, Eq. (91) can be re-expressed as follows:

$$f(p_{\perp}, y) \approx |N^{+}(p_{\perp})|^2 \left( C_0(p_{\perp}, y) + (1 - y)C_1(p_{\perp}, y) + (1 - y)^2 C_2(p_{\perp}, y) \right) \quad (109)$$

where,

$$\begin{aligned}
C_0(p_\perp, y) &= 4y^2|\Gamma_2|^2\left(1 + p_\perp^2 + E_0\tau(E_0\tau + \sqrt{1 + p_\perp^2 + E_0^2\tau^2})\right) \\
C_1(p_\perp, y) &= -\frac{4yE_0\tau|\Gamma_1\overline{\Gamma_2}|(1 + p_\perp^2)}{\sqrt{1 + p_\perp^2 + E_0^2\tau^2}} \cos(\Upsilon) \\
C_2(p_\perp, y) &= 4E_0^2\tau^2(1 + p_\perp^2)|\Gamma_1|^2 \frac{(-E_0\tau + \sqrt{1 + p_\perp^2 + E_0^2\tau^2})}{(1 + p_\perp^2 + E_0^2\tau^2)^{3/2}} \\
&\quad + \left( -\frac{8|\Gamma_1\overline{\Gamma_2}|(1 + p_\perp^2)E_0\tau(1 + p_\perp^2 + E_0\tau\sqrt{1 + p_\perp^2 + E_0^2\tau^2})}{(1 + p_\perp^2 + E_0^2\tau^2)^{3/2}} \right. \\
&\quad + 8|\Gamma_1\overline{\Gamma_2}|E_0\tau y\left(5E_0\tau - \frac{E_0^2\tau^2}{\sqrt{1 + p_\perp^2 + E_0^2\tau^2}} + 2\sqrt{1 + p_\perp^2 + E_0^2\tau^2} + \frac{E_0^4\tau^2[3 + \tau^2(1 + p_\perp^2 + E_0^2\tau^2)]}{(1 + p_\perp^2 + E_0^2\tau^2)^{3/2}} \right. \\
&\quad \left. \left. + E_0^3\tau^3 \frac{(-1 + \tau^2(1 + p_\perp^2 + E_0^2\tau^2))}{1 + p_\perp^2 + E_0^2\tau^2} \right) + \frac{8y^2E_0\tau\Gamma_1\overline{\Gamma_2}(1 + E_0^2\tau^4)}{4 + \tau^2(1 + p_\perp^2 + E_0^2\tau^2)} (4 + E_0\tau^3\sqrt{1 + p_\perp^2 + E_0^2\tau^2}) \right. \\
&\quad \left. (E_0\tau + \sqrt{1 + p_\perp^2 + E_0^2\tau^2}) \right) \cos(\Upsilon) \tag{110}
\end{aligned}$$

Figure 19 shows the  $p_\perp$ -momentum evolution of individual components defined in eq. (109) from initial to final stages of pair creation. The profile of  $(1 - y)^2C_2$  exhibits substructure, with its maximum peak located at  $p_\perp \approx \pm 0.65[m]$  and a valley near  $p_\perp \approx \pm 0.25[m]$ , as observed at time  $t = 13[m^{-1}]$  (see Fig. 19(a)). Similarly, the feature shown by  $(1 - y)C_1$  has peaks at  $p_\perp = \pm 0.25[m]$ , but its peak value in this case is too small compared to  $(1 - y)^2C_2$ . As time progresses, this substructure can change according to the expression Eq.(110). Therefore, as seen in Fig. 17(b) at  $t = 17[m^{-1}]$ , the profiles of  $(1 - y)^2C_2$  and  $(1 - y)C_1$  change with time, with the peak magnitude of  $(1 - y)^2C_2$  still dominating over other terms.

$$\begin{aligned}
C_1(p_\perp, y) &\approx \frac{2yE_0(1 + E_0\tau(E_0\tau + \sqrt{1 + E_0^2\tau^2}))}{(1 + E_0^2\tau^2)^{3/2}} e^{\pi\tau(E_0\tau - \sqrt{1 + E_0^2\tau^2})} \exp\left(\frac{p_\perp^2}{2}\tau\left(\frac{2E_0^2\tau}{1 + E_0^2\tau^2} - \frac{E_0 + \pi}{\sqrt{1 + E_0^2\tau^2}}\right)\right) \cos(\Upsilon) \\
C_2(p_\perp, y) &\approx 4E_0^2\tau^2(1 + p_\perp^2) \frac{(-E_0\tau + \sqrt{1 + p_\perp^2 + E_0^2\tau^2})}{(1 + p_\perp^2 + E_0^2\tau^2)^{3/2}} |\Gamma_1|^2 + \frac{4E_0e^{-\Lambda\frac{p_\perp^2}{2}} \cos(\Upsilon)}{\tau(1 + E_0^2\tau^2)^{7/2}} \left(3E_0^4\tau^5(3 + 8E_0^2) + 13E_0^6\tau^7 \right. \\
&\quad + 6E_0^8\tau^9 + 12E_0\sqrt{1 + E_0^2\tau^2} + 4E_0\tau^2(1 + 7E_0^2)\sqrt{1 + E_0^2\tau^2} + 8E_0^3\tau^4(1 + 3E_0^2)\sqrt{1 + E_0^2\tau^2} \\
&\quad \left. + 10E_0^5\tau^6\sqrt{1 + E_0^2\tau^2} + 6E_0^7\tau^8\sqrt{1 + E_0^2\tau^2}\right) \tag{111}
\end{aligned}$$



where,

$$\begin{aligned}
\Lambda = & (\tau(48E_0^2 - 1) + E_0^2\tau^3(136E_0^2 - 5) + E_0^4\tau^5(9 + 88E_0^2) + 29E_0^6\tau^7 + 16E_0^8\tau^9 + 24E_0\sqrt{1 + E_0^2\tau^2} \\
& + 64E_0^3\tau^2\sqrt{1 + E_0^2\tau^2} + 8E_0^3\tau^4(11E_0^2 - 1)\sqrt{1 + E_0^2\tau^2} + 8E_0^5\tau^6\sqrt{1 + E_0^2\tau^2} \\
& + 16E_0^7\tau^8\sqrt{1 + E_0^2\tau^2}) / ((1 + E_0^2\tau^2)(\tau + 16E_0^2\tau + E_0^2\tau^3(3 + 40E_0^2) + 3E_0^4\tau^5(3 + 8E_0^2) + 13E_0^6\tau^7 \\
& + 6E_0^8\tau^9 + 12E_0\sqrt{1 + E_0^2\tau^2} + 4E_0\tau^2(1 + 7E_0^2)\sqrt{1 + E_0^2\tau^2} + 8E_0^3\tau^4(1 + 3E_0^2)\sqrt{1 + E_0^2\tau^2} \\
& + 10E_0^5\tau^6\sqrt{1 + E_0^2\tau^2} + 6E_0^7\tau^8\sqrt{1 + E_0^2\tau^2}) \tag{112}
\end{aligned}$$

The change in the shape of  $(1 - y)^2C_2$  and  $(1 - y)C_1$  can be understood as  $\cos(\Upsilon)$  function that presents in the relation Eq.(111). From Eq.(111) we easily see that  $C_1(p_\perp, y)$  and  $C_2(p_\perp, y)$  shows single peak Gaussian-like profile with the cosine function and its behavior depends on the field parameters. We now analyze the  $C_2(p_\perp, y)$  function that shows the complicated substructure that changes with time. From Eq.(110) first term shows a complicated substructure having two peaks at  $p_\perp \approx \pm 1.5[m]$  and dip at the  $p_\perp \approx 0$ . This structure does not change with time but the second term plays crucial role whose depends the shape of profile on the time since  $\cos(\Upsilon)$  factor and its amplitude function gives multi-peak substructure behavior. We again look to the cosine argument to understand this substructure behavior of the spectra for that we approximate the cosine argument and take the term up to  $p_\perp^2$  and neglect higher orders.

$$\begin{aligned}
\Upsilon \approx & E_0\tau^2 \ln(1 + (E_0\tau + \sqrt{1 + E_0^2\tau^2})2E_0\tau) + \tau \ln\left(\frac{(1 - y)}{\sqrt{1 + E_0^2\tau^2}}\right) \sqrt{1 + E_0^2\tau^2} \\
& + \frac{p_\perp^2\tau}{2\sqrt{1 + E_0^2\tau^2}} \ln\left(\frac{(1 - y)}{1 + E_0^2\tau^2}\right) \tag{113}
\end{aligned}$$

It shows behavior is symmetric about the origin, which can be understood as the presence of only  $p_\perp^2$  and the absence of  $p_\perp$  linear term in comparison to longitudinal momentum case as we discussed in section IV B 1. One more thing we can notice is that at  $p_\perp = 0$  near this value the  $\cos(\Upsilon)$  function behavior drastically changes with time due to the presence of time-dependent term  $\ln(1 - y)$ . The oscillation frequency also depends on the  $p_\perp$  which means frequency increase as transverse momentum value increases. But the amplitude function plays a role here which gives the Gaussian envelope to the cosine function as discussed previously and within the width of the Gaussian profile oscillation survives and is seen in the spectrum. Fig. 19(c) shows that  $C_0$  term dominates over other terms. We still observed substructure in the first and second-order terms  $(1 - y)C_1$  and  $(1 - y)^2C_2$  profile whose magnitude drastically decreases but these terms still have an impact on  $f(p_\perp, t)$  at this time. The term  $C_0$  shows a smooth Gaussian profile having a peak at

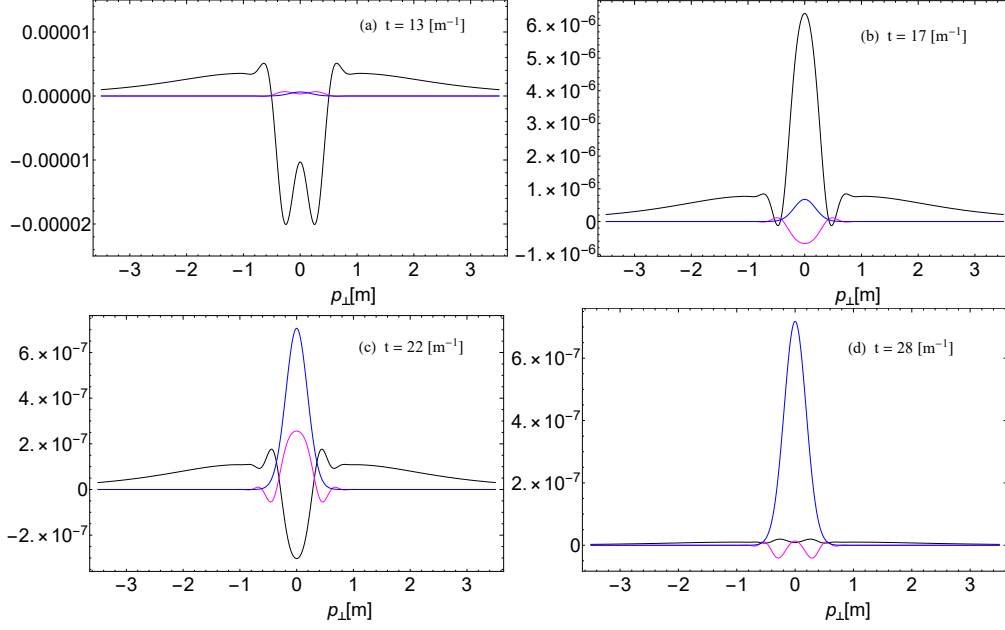


Figure 19: The zeroth, first and second order terms as a function of the longitudinal momentum for different times. Blue curve :  $C_0$ , Magenta curve :  $(1 - y)C_1$  and Black curve:  $(1 - y)^2C_2$ . The field parameters are  $E_0 = 0.2E_c$  and  $\tau = 10[m^{-1}]$ .

$p_{\perp} = 0$  and shape does not change with time. At  $t = 32[m^{-1}]$ , the first and second order suppressed and impression on only zeroth order term able to explain the features of the spectra.

On carefully examining the different terms  $C_0$ ,  $(1 - y)C_1$  and  $(1 - y)^2C_2$  as defined in Eq.110, we can say that in initial TMS behavior qualitatively explained by the first and second order term. But up to  $t \approx 2\tau$ , the function  $(1 - y)^2C_2$  qualitatively explains the non-zero peak and sub-structure near the transient region. As discussed above, this substructure is due to the time-dependent  $\cos(\Upsilon)$  function. Since the magnitude of  $(1 - y)^2C_2$  and  $(1 - y)C_1$  decreases as time progresses and is finally suppressed at  $y \rightarrow 1$  in comparison to other terms of distribution function as result substructure nearly disappears(see Fig.17). In the late time limit,  $f(p_{\perp})$  is governed mainly by zeroth-order term,  $C_0$  due to which spectra only show the single peak smooth profile. For that, we can further derive an asymptotic expression for the transverse momentum distribution function in the limit  $y \rightarrow 1(t \rightarrow \infty)$ . From the Eq.109 we can write as:

$$f(p_{\perp}, y \rightarrow 1) \approx |N^+(p_{\perp})|^2 C_0(p_{\perp}) \quad (114)$$

By lengthy calculation, as we do for longitudinal momentum case, we found an expression for the

transverse momentum distribution function for asymptotic time as follows:

$$f(p_{\perp}) \approx 2e^{2\pi\tau(E_0\tau - \sqrt{1+E_0^2\tau^2})} \exp\left(\frac{-\pi p_{\perp}^2 \tau}{\sqrt{1+E_0^2\tau^2}}\right) \quad (115)$$

the above Eq.(115) clearly shows that in the REPP stage transverse distribution function,  $f(p_{\perp})$  have invariable Gauss-like distribution whose half-width is defined by the field strength,  $E_0$  and pulse duration  $\tau$ .

## V. CONCLUSION

We have conducted a detailed analysis of the electron-positron pair creation from the vacuum under the influence of a time-dependent Sauter pulse electric field. We computed the one-particle distribution function in momentum space for the Sauter-pulse electric field with the help of the exact analytic solution for the mode function. We develop an analytical theory that is valid for the finite times  $t > \tau$ . In particular, we find an analytical expression for one-particle distribution function in the power series of the small parameter  $(1 - y)$ . The interesting dynamical features of the momentum distribution function at finite times are attributed to the function that appears in this expansion. We have further elaborated on this aspect of the finite-time behavior of the longitudinal and transverse momentum spectra. We investigated the temporal evolution of the one-particle distribution function. Our investigation reveals that the process of transition from initially virtual particles to real particles occurs in three distinct stages, which crucially depend on the longitudinal and transverse modes in momentum space. Moreover, we have quantified the initiation of the REPP stage, determined by the momentum value, with higher momenta resulting in narrower oscillations in the transient region. We meticulously examined the LMS and TMS to understand the momentum-dependent behavior during these stages. In the LMS, one interesting feature at the beginning of the REPP stage is that the Longitudinal momentum distribution function exhibits an oscillating structure as imprints of a quantum signature at the finite time where the electric field is nearly zero, which can be understood in the Dynamical Tunneling picture. The two-peaked structure in which the central Gaussian-peak structure has onset oscillation, and this quantum interference pattern evolves and fades away. Based on this observation, we identified three distinct time scales associated with this behavior. Consequently, we concluded that these oscillations are prominent in the LMS at the Compton time scale during the formation of electron-positron pairs. Additionally, we investigated the impact of different electric field strengths ( $E_0$ ) on the duration of the interference pattern's formation and disappearance. Subsequently, we examined whether or

not the oscillation structure behavior at finite time explicitly depends on the Keldysh parameter ( $\gamma$ ). Remarkably, we found that for two different configurations of parameters ( $E_0, \tau$ ) under the same  $\gamma = 1$ , distinct behaviors were observed due to their placement in the intermediate regime of pair production. In the multiphoton regime, for  $\gamma = 2.5$ , we explored the time evolution of LMS in different stages of pair production, and the spectrum shows the splitting of a smooth uni-modal structure into a multi-modal Gaussian structure near the REPP region, after which it merges into a single peak Gaussian profile at the asymptotic time limit. We also derived approximate expressions for the single-particle momentum distribution function at finite times. Utilizing these expressions, we unveiled that the LMS structure mainly comprises three distinct functional behaviors. The second-order term dominantly governs the early times, while combining the first and zeroth-order terms leads to the central peak structure with onset oscillation. The first-order term contributes to oscillations, owing to the presence of a Gaussian envelope with oscillation, but its amplitude diminishes with time, resulting in a smooth spectrum profile in late time. Furthermore, we investigated the role of vacuum polarization,  $u(p_{\parallel}, t)$ , and its counterpart,  $v(p_{\parallel}, t)$ , by plotting their time evolution. In the REPP region, both  $u(p_{\parallel}, t)$  and  $v(p_{\parallel}, t)$  exhibit nearly identical oscillations with the same amplitude, and this oscillation amplitude decays for higher  $p_{\parallel}$  values. This observation implies that the qualitative nature of the vacuum polarization function is significantly influenced by the longitudinal momentum. To elucidate this further, we plotted the LMS of  $u(p_{\parallel}, t)$  and  $v(p_{\parallel}, t)$ . These plots reveal two distinct patterns emerging at the start of the REPP stage. One pattern exhibits a Gaussian-like structure, while the other displays a deformed oscillating profile within the Gaussian envelope. These oscillations, exhibiting varying amplitudes, were confined to a small window of longitudinal momentum ( $-1 < p_{\parallel} < 1$ ). Over time, the regular oscillations of  $u(p_{\parallel}, t)$  and  $v(p_{\parallel}, t)$  became balanced, as explicitly observed in the plot of the LMS of the created particles for late time, where the oscillating behavior was absent due to the equilibrium between  $u(p_{\parallel}, t)$  and  $v(p_{\parallel}, t)$ . As we recognize the pivotal roles of  $u(p_{\parallel}, t)$  and  $v(p_{\parallel}, t)$  functions in accelerating (creation of  $e^-$ ) and decelerating (annihilation of  $e^-$ ) electrons, respectively, the observed oscillations in the LMS of  $f(p_{\parallel}, p_{\perp}, t)$  at finite times can be attributed to the characteristic behavior imprints of these functions, resulting from the acceleration and deceleration of electrons in momentum representation, which manifests as the observed oscillating structure. Next, we also discuss the influence of transverse momentum on LMS, which diminishes the value of  $f(p_{\parallel})$  and smooths out the oscillation for higher  $p_{\perp}$  values. Moreover, we emphasized that these oscillations, seen in the late REPP stage as transverse momentum increases and also impact the formation time of pairs.

Finally, we study the dynamics of TMS, uncovering interesting results that have received limited

attention from other authors, particularly in the context of the Sauter pulsed electric field. We observe fluctuating substructures that undergo regular changes in the QEPP and transient region depending on momentum value. This behavior of substructures during this stage is also influenced by longitudinal momentum, resulting in distinct substructures in the spectrum at a given time. This finding indicates that the longitudinal and transverse momentum is related to each other during particle-antiparticle formation quantitatively and qualitatively. At the beginning of the REPP region, that substructure disappears. The shape of the spectrum becomes an invariable Gauss-like profile and is not affected by the longitudinal momentum but its peak value still depends on it during the REPP stage. This contrast highlights the dynamic evolution of substructures in earlier stages, contrasting with the stable Gaussian-like structure observed in the REPP stage. A similar intriguing behavior in the transverse momentum distribution has been observed in the works by Krajewska et al. [81] and Bechler et al. [82], depending on the specifics of the electric field parameters. These studies highlight a fascinating characteristic of the transverse distribution function peak that occurs at non-zero  $p_{\perp}$ -value depending on the frequency. This observation prompts questions about the feasibility of pair formation through tunneling theory, particularly considering the significant distribution function values at non-zero transverse momentum for low frequencies. For our case the tunneling theory for TMS remains applicable. Since, we only observe off-axis maxima for TMS in the initial stages of the dynamics. As we approach the asymptotic state, the maximum of the momentum distribution moves to  $p_{\perp} = 0$ , potentially aligning with tunneling theory.

Although studying the LMS and TMS of created quasi-particles at various dynamical stages shows a critical dependence on longitudinal and transverse momentum, it also brings attention to the intriguing physics behind the behavior of the vacuum in this finite-time scenario for the pair production process.

## VI. ACKNOWLEDGMENTS

Deepak gratefully acknowledge the financial support from Homi Bhabha National Institute (HBNI) for carrying out this research work.

---

[1] P. A. M. Dirac, Proc. Roy. Soc. Lond. A **117**, 610 (1928).

[2] F. Sauter, Z. Phys. **69**, 742 (1931).

- [3] W. Heisenberg and H. Euler, Z. Phys. **98**, 714 (1936), physics/0605038.
- [4] J. S. Schwinger, Phys. Rev. **82**, 664 (1951).
- [5] F. Sauter, Z. Phys. **73**, 547 (1932).
- [6] W. Greiner, B. Müller, and J. Rafelski, *Quantum Electrodynamics of Strong Fields* (Springer Berlin Heidelberg, Berlin, Heidelberg, 1985).
- [7] L. Parker, Phys. Rev. Lett. **21**, 562 (1968).
- [8] S. W. Hawking, Commun. Math. Phys. **43**, 199 (1975), [Erratum: Commun.Math.Phys. 46, 206 (1976)].
- [9] M. K. Parikh and F. Wilczek, Phys. Rev. Lett. **85**, 5042 (2000), hep-th/9907001.
- [10] W. G. Unruh, Phys. Rev. D **14**, 870 (1976).
- [11] S. P. Kim, Int. J. Mod. Phys. D **25**, 1645005 (2016), 1602.05336.
- [12] V. S. Popov, Zh. Eksp. Teor. Fiz. **61**, 1334 (1971).
- [13] M. S. Marinov and V. S. Popov, Fortsch. Phys. **25**, 373 (1977).
- [14] L. V. Keldysh, J. Exp. Theor. Phys. **20**, 1307 (1965).
- [15] A. I. Nikishov, Zh. Eksp. Teor. Fiz. **57**, 1210 (1969).
- [16] N. B. Narozhnyi and A. I. Nikishov, Yad. Fiz. **11**, 1072 (1970).
- [17] A. Nikishov, arXiv preprint hep-th/0111137 (2001).
- [18] E. Brezin and C. Itzykson, Phys. Rev. D **2**, 1191 (1970).
- [19] V. G. Bagrov, D. M. Gitman, and S. M. Shvartsman, Zh. Eksp. Teor. Fiz. **68**, 392 (1975).
- [20] V. M. Mostepanenko and V. M. Frolov, Yad. Fiz. **19**, 885 (1974).
- [21] N. B. Narozhnyi and A. I. Nikishov, Zh. Eksp. Teor. Fiz., v. 65, no. 3, pp. 862-874 (1973), URL <https://www.osti.gov/biblio/4400849>.
- [22] J. Andruszkow et al. (TESLA), Phys. Rev. Lett. **85**, 3825 (2000), physics/0006010.
- [23] T. Heinzl and A. Ilderton, Eur. Phys. J. D **55**, 359 (2009), 0811.1960.
- [24] G. V. Dunne, Eur. Phys. J. D **55**, 327 (2009), 0812.3163.
- [25] E. Khazanov and et al., High Power Laser Science and Engineering p. 1–77 (2023).
- [26] D. Allor, T. D. Cohen, and D. A. McGady, Phys. Rev. D **78**, 096009 (2008), 0708.1471.
- [27] G. L. Klimchitskaya and V. M. Mostepanenko, Phys. Rev. D **87**, 125011 (2013), 1305.5700.
- [28] F. Fillion-Gourdeau and S. MacLean, Phys. Rev. B **92**, 035401 (2015).
- [29] Y. Kluger, E. Mottola, and J. M. Eisenberg, Phys. Rev. D **58**, 125015 (1998), hep-ph/9803372.
- [30] M. V. Berry and K. E. Mount, Rept. Prog. Phys. **35**, 315 (1972).
- [31] L. Parker, Phys. Rev. **183**, 1057 (1969).

- [32] C. Lueders and J. E. Roberts, *Commun. Math. Phys.* **134**, 29 (1990).
- [33] B. S. DeWitt, *Phys. Rept.* **19**, 295 (1975).
- [34] E. Mottola, *Phys. Rev. D* **31**, 754 (1985).
- [35] S. P. Gavrilov and D. M. Gitman, *Phys. Rev. D* **53**, 7162 (1996), hep-th/9603152.
- [36] J. Hallin and P. Liljeborg, *Phys. Rev. D* **52**, 1150 (1995), hep-th/9412188.
- [37] H. M. Fried and R. P. Woodard, *Phys. Lett. B* **524**, 233 (2002), hep-th/0110180.
- [38] J. Avan, H. M. Fried, and Y. Gabellini, *Phys. Rev. D* **67**, 016003 (2003), hep-th/0208053.
- [39] S. A. Smolyansky, A. V. Prozorkevich, S. M. Schmidt, D. Blaschke, G. Roepke, and V. D. Toneev, *Int. J. Mod. Phys. E* **7**, 515 (1998), nucl-th/9709057.
- [40] S. P. Kim and D. N. Page, *Phys. Rev. D* **65**, 105002 (2002), hep-th/0005078.
- [41] I. K. Affleck, O. Alvarez, and N. S. Manton, *Nucl. Phys. B* **197**, 509 (1982).
- [42] R. Alkofer, M. B. Hecht, C. D. Roberts, S. M. Schmidt, and D. V. Vinnik, *Phys. Rev. Lett.* **87**, 193902 (2001), nucl-th/0108046.
- [43] C. D. Roberts, S. M. Schmidt, and D. V. Vinnik, *Phys. Rev. Lett.* **89**, 153901 (2002), nucl-th/0206004.
- [44] R. Dabrowski and G. V. Dunne, *Phys. Rev. D* **94**, 065005 (2016), 1606.00902.
- [45] A. Ilderton, *Phys. Rev. D* **105**, 016021 (2022), 2108.13885.
- [46] A. Di Piazza, *Phys. Rev. D* **70**, 053013 (2004).
- [47] M. Melike, X. Bai-Song, and D. Sayipjama, *Communications in Theoretical Physics* **57**, 422 (2012).
- [48] T. C. Adorno, S. P. Gavrilov, and D. M. Gitman, *Int. J. Mod. Phys. A* **32**, 1750105 (2017), 1512.01288.
- [49] G. V. Dunne and T. Hall, *Phys. Rev. D* **58**, 105022 (1998), hep-th/9807031.
- [50] A. B. Balantekin, J. E. Seger, and S. H. Fricke, *Int. J. Mod. Phys. A* **6**, 695 (1991).
- [51] A. I. Nikishov, *Phys. Atom. Nucl.* **67**, 1478 (2004), hep-th/0304174.
- [52] P. Levai and V. Skokov, *Phys. Rev. D* **82**, 074014 (2010), 0909.2323.
- [53] A. A. Grib, S. G. Mamayev, and V. M. Mostepanenko, *Vacuum quantum effects in strong fields* (Friedman Laboratory Publ. St. Petersburg, St. Petersburg, 1994).
- [54] A. A. Grib, V. M. Mostepanenko, and V. M. Frolov, *Theoretical and Mathematical Physics* **13**, 1207 (1972), ISSN 1573-9333, URL <https://doi.org/10.1007/BF01036146>.
- [55] L. H. Ryder, *Quantum Field Theory* (Cambridge University Press, 1996), ISBN 978-0-521-47814-4, 978-1-139-63239-3, 978-0-521-23764-2.
- [56] R. P. Feynman and M. Gell-Mann, *Phys. Rev.* **109**, 193 (1958).
- [57] S. M. Schmidt, D. Blaschke, G. Ropke, S. A. Smolyansky, A. V. Prozorkevich, and V. D. Toneev, *Int. J. Mod. Phys. E* **7**, 709 (1998), hep-ph/9809227.

- [58] K. Nakajima, AIP Conf. Proc. **737**, 614 (2004).
- [59] D. B. Blaschke, A. V. Prozorkevich, G. Ropke, C. D. Roberts, S. M. Schmidt, D. S. Shkirmanov, and S. A. Smolyansky, Eur. Phys. J. D **55**, 341 (2009), 0811.3570.
- [60] F. Hebenstreit, R. Alkofer, and H. Gies, Phys. Rev. D **82**, 105026 (2010), 1007.1099.
- [61] C. Kohlfurst, M. Mitter, G. von Winckel, F. Hebenstreit, and R. Alkofer, Phys. Rev. D **88**, 045028 (2013), 1212.1385.
- [62] F. Gelis and N. Tanji, Prog. Part. Nucl. Phys. **87**, 1 (2016), 1510.05451.
- [63] I. Bialynicki-Birula and L. Rudnicki (2011), 1108.2615.
- [64] M. Abramowitz and I. A. Stegun, *Handbook of Mathematical Functions with Formulas, Graphs, and Mathematical Tables* (Dover, New York, 1964), ninth dover printing ed.
- [65] D. B. Blaschke, V. V. Dmitriev, G. Ropke, and S. A. Smolyansky, Phys. Rev. D **84**, 085028 (2011), 1105.5397.
- [66] C. Banerjee and M. P. Singh, Phys. Rev. D **105**, 076021 (2022), 1807.06951.
- [67] C. Banerjee and M. P. Singh, Phys. Rev. D **100**, 056016 (2019), 1809.06901.
- [68] D. B. Blaschke, S. A. Smolyansky, A. Panferov, and L. Juchnowski, in *Quantum Field Theory at the Limits: from Strong Fields to Heavy Quarks* (2017), pp. 1–23, 1704.04147.
- [69] A. M. Fedotov, E. G. Gelfer, K. Y. Korolev, and S. A. Smolyansky, Phys. Rev. D **83**, 025011 (2011), 1008.2098.
- [70] S. A. Smolyansky, D. B. Blaschke, A. V. Chertilin, G. Roepke, and A. V. Tarakanov (2010), 1012.0559.
- [71] D. B. Blaschke, A. V. Prozorkevich, C. D. Roberts, S. M. Schmidt, and S. A. Smolyansky, Phys. Rev. Lett. **96**, 140402 (2006), nucl-th/0511085.
- [72] D. B. Blaschke, G. Ropke, S. M. Schmidt, S. A. Smolyansky, and A. V. Tarakanov, Contrib. Plasma Phys. **51**, 451 (2011), 1006.1098.
- [73] D. B. Blaschke, G. Ropke, V. V. Dmitriev, S. A. Smolyansky, and A. V. Tarakanov (2011), 1101.6021.
- [74] A. Di Piazza, K. Z. Hatsagortsyan, and C. H. Keitel, Phys. Rev. Lett. **97**, 083603 (2006), hep-ph/0602039.
- [75] S. M. Schmidt, D. Blaschke, G. Ropke, A. V. Prozorkevich, S. A. Smolyansky, and V. D. Toneev, Phys. Rev. D **59**, 094005 (1999), hep-ph/9810452.
- [76] L. V. Keldysh, Herald of the Russian Academy of Sciences **86**, 413 (2016), ISSN 1555-6492, URL <https://doi.org/10.1134/S1019331616060113>.
- [77] D. Sah and M. P. Singh, arXiv e-prints arXiv:2301.06545 (2023), 2301.06545.
- [78] C. K. Dumlu and G. V. Dunne, Phys. Rev. D **83**, 065028 (2011), 1102.2899.



- [79] H. K. Avetissian, A. K. Avetissian, G. F. Mkrtchian, and K. V. Sedrakian, *Phys. Rev. E* **66**, 016502 (2002).
- [80] H. Taya, H. Fujii, and K. Itakura, *Phys. Rev. D* **90**, 014039 (2014), 1405.6182.
- [81] K. Krajewska and J. Z. Kamiński, *Phys. Rev. A* **100**, 012104 (2019), 1811.07528.
- [82] A. Bechler, F. Cajiao Vélez, K. Krajewska, and J. Z. Kamiński, *Acta Phys. Polon. A* **143**, S18 (2023), 2306.07668.